

Variability of Narrow, Associated Absorption Lines in Moderate- and Low-Redshift Quasars

John H. Wise, Michael Eracleous, Jane C. Charlton, and Rajib Ganguly¹

Department of Astronomy and Astrophysics, 525 Davey Laboratory, The Pennsylvania State University, University Park, PA 16802

jwise, mce, charlton, ganguly@astro.psu.edu

ABSTRACT

We present the results of a search for variability in the equivalent widths (EWs) of narrow, associated ($|\Delta v| \leq 5,000 \text{ km s}^{-1}$) absorption lines found in the UV spectra of $z \leq 1.5$ quasars. The goal of this search was to use variability as a means of identifying absorption lines arising in gas that is intrinsic to the quasar central engine. We have compared archival *HST*/FOS spectra of quasars with recent spectra obtained as part of our own snapshot survey of the same objects with STIS. The intervals between observations are 4–10 years. We primarily focused on the C IV absorption lines, although we also studied other lines available in the same spectra (e.g., Ly α , N V, O VI). Our main result is that 4 out of 15 quasars, or 4 out of 19 associated absorption systems, contained variable narrow absorption lines, which are indicative of intrinsic absorption. We conclude that a minimum of 21% of the associated absorption-line systems are variable. Because not all systems will have necessarily varied, this is a lower limit on this fraction and it is consistent with previous estimates based on variability, partial coverage analysis, or statistical arguments. If we interpret the upper limits on the variability time scale as upper limits on the recombination time of the absorber, we constrain the density of the absorber to be $n_e > 3000 \text{ cm}^{-3}$ and its distance from the ionizing source to be $R \lesssim 100 \text{ pc}$. Moreover, we are now able to pick out specific intrinsic absorption-line systems to be followed up with high-dispersion spectroscopy in order to constrain the geometry, location, and physical conditions of the absorber. We briefly illustrate how followup studies can yield such constraints by means of a simulation.

Subject headings: galaxies: active – quasars: absorption lines – quasars: general – accretion

¹Current address: Space Telescope Science Institute, 3700 San Martin Drive, Baltimore, MD 21218; e-mail ganguly@stsci.edu.

1. Introduction

The spectra of quasars often show a plethora of absorption lines, some of which arise in gas that is somehow associated with the quasar, while others arise in systems that are unrelated to the quasar (e.g., galaxies along the line of sight at a much lower redshift). A recent summary of the properties of intrinsic absorption lines (and of their nomenclature) can be found in Hamann & Sabra (2004). The properties of absorbing gas that is intimately associated with the quasar are of particular interest in studies of quasar central engines because they provide constraints and insights on the accretion process that powers the central engine (such gaseous systems are referred to hereafter as “intrinsic systems” and the lines they produce as “intrinsic absorption lines”). The predominance of *blueshifts* among intrinsic absorption lines, suggests that the gas has the form of an outflowing wind, which in turn makes it an important component of the accretion process. More specifically, the wind can be an important mechanism for extracting angular momentum from the accretion flow, allowing accretion to proceed. Thus the study of intrinsic absorption lines can provide information on how common winds are, as well as estimates or limits on the mass outflow rates, which can serve as constraints on models for the accretion flow. Studying the dynamics and conditions in the absorber also allows us to explore its connection to the broad-emission line gas. In addition, intrinsic absorption lines trace the evolution of quasar outflows, and presumably the cosmic evolution in quasar fueling rate (see, for example, the discussion by Ganguly et al. 2001a).

Before any detailed study of the physical conditions in intrinsic absorption systems can be carried out, one must identify intrinsic absorption lines with certainty, a task that can be rather difficult in practice. In the case of *broad* absorption lines (BALs), whose widths exceed 2,000 km s⁻¹ by definition and often exceed 10,000 km s⁻¹ in practice (e.g., Turnshek 1987; Turnshek et al. 1988; Weymann et al. 1991), a good case can be made that the absorbing gas has the form of a fast accretion-disk wind (see, for example, Murray et al. 1995; Proga et al. 2000). Similarly, narrow absorption lines (hereafter NALs; those whose widths are small enough that the strong UV resonance doublets, such as C IV, Si IV, and N V, are resolved, i.e., FWHM \lesssim 300 km s⁻¹), with $z_a \ll z_e$ (where z_a and z_e are the absorption emission redshifts, respectively), or more specifically with velocities of 18,000 km s⁻¹ or more, relative to the quasar, are likely to arise in gas that is distant from and not related to the quasar (see Weymann et al. 1979a). This is not guaranteed to always be the case, however, since a number of NALs with $z_a \ll z_e$ have been found to vary, which suggests that the absorber is closely related to the quasar (e.g., in Q2343+125 and PG 2302+029; Hamann, Barlow, & Junkkarinen 1997b; Jannuzi 2002). Moreover the statistical study of Richards et al. (1999) found that dN/dz (the number of absorption-line systems per object per unit redshift) in the range $1.6 < z < 3.5$ depends on quasar optical and radio properties. More specifically, they find a statistical excess of absorbers in the velocity range $-15,000$ km s⁻¹ to $-65,000$ km s⁻¹ in optically luminous quasars ($M_V < -27.0$), relative to quasars of lower luminosities.

In the velocity range $\Delta v \lesssim -18,000$ km s⁻¹, dN/dz is significantly higher than the expected density of intervening absorbers (Weymann et al. 1979a). In fact, at $\Delta v < -5,000$ km s⁻¹ as many as 2/3 of the absorption systems could be intrinsic to the quasars (see, for example, Aldcroft,

Bechtold, & Elvis 1994, and references therein). This excess of absorbers could be attributed to a combination of galaxies in a cluster surrounding the quasar and parcels of gas ejected from the quasar in the form of a wind (Weymann et al. 1979a; Anderson et al. 1987). The NALs of the latter type are particularly interesting and deserving of detailed study in the context of quasar central engines because they appear to be ubiquitous in quasar spectra (e.g., Anderson et al. 1987) and their frequency appears to evolve with redshift (Ganguly et al. 2001a). However, judging which particular NALs arise in gas intrinsic to the quasar is rather challenging.

This leads us to undertake this study, whose goal is to identify intrinsic NALs in moderate- and low-redshift quasars ($z \leq 1.5$) based on their variability. This is a relatively economical technique discussed by Barlow & Sargent (1997). We focus on absorption lines that are within $5,000 \text{ km s}^{-1}$ of the quasar redshift; such absorption-line systems are conventionally regarded as “associated” with the quasar, following Foltz et al. (1986). Although many statistical studies have been conducted to determine the frequency of intrinsic absorbers relative to all NAL systems, only a handful of specific absorption systems have been identified as truly intrinsic. Moreover, variability information is sparse. Barlow et al. (1997) estimated that 30% of NALs are variable to some unspecified level, while specific variable systems in high-redshift quasars have been studied in detail by Hamann et al. (1995), Hamann et al. (1997b), and more recently by Narayanan et al. (2004).

To search for variability among associated NALs in $z \leq 1.5$ quasars we have carried out a snapshot survey with the Space Telescope Imaging Spectrograph (STIS) on the *Hubble Space Telescope* (*HST*). We chose quasars which had already been observed with the *HST*’s Faint Object Spectrograph (FOS) and were known to have associated C IV, N V, or O VI NALs. The specific goals of this survey were to:

- (a) Determine the fraction of variable NALs among the associated NALs observed in low-redshift quasars. This provides a *lower limit* on the fraction of associated NALs that are truly intrinsic, since not all intrinsic NALs will have varied while we were observing them. The results obtained for high-redshift quasars, observed from the ground, need not apply at low redshifts, since the frequency of associated NALs evolves with redshift (Ganguly et al. 2001a).
- (b) Increase the number of confirmed intrinsic absorbers so that more detailed followup studies can be carried out on *specific* systems.

We describe the observations and data analysis methods in §2 while in §3 we present the results. In §4 we discuss the implications of NAL variability, we comment on individual objects, and suggest future, followup work on NAL quasars.

2. Observations and Data Analysis

A sample of 15 quasars with associated NALs were surveyed for variability primarily in the following UV absorption lines: O VI $\lambda\lambda 1032, 1038$, H I $\lambda 1215$, N V $\lambda\lambda 1239, 1243$, and C IV $\lambda\lambda 1548, 1551$, but also in the Si II $\lambda\lambda 1190, 1193$, Si II $\lambda 1260$, and Si III $\lambda 1207$ lines. The

journal of observations is given in Table 1, which also includes information for both the first-epoch FOS observations and the second-epoch STIS observations. We have paid particular attention to collecting accurate redshifts from the literature, since these are important in determining the velocities of absorption lines relative to the rest-frame of the quasar, and whether a specific absorption system is blueshifted or redshifted relative to the quasar. Thus, we have examined the original redshift reports for all of our target quasars and considered their uncertainties before adopting the reported values. In §4.2, we give a brief discussion of our adopted redshift for specific objects. In Table 1, we list the redshifts we have adopted along with their uncertainties, where available, and the source of the information. In cases where an uncertainty is not quoted, we expect that the uncertainty is of order a few in the last decimal place given. An uncertainty in the redshift, δz , translates into an uncertainty in the velocity of an absorption system relative to the quasar rest-frame of $\delta v \sim c \delta z / (1 + z) < c \delta z$. Redshift uncertainties of $\delta z \lesssim 10^{-4}$ are comparable to redshift errors arising from heliocentric corrections; since the papers reporting the redshifts rarely report the application of heliocentric corrections, an additional uncertainty of up to 30 km s^{-1} , may have to be taken into account.

As Table 1 shows, not all desirable lines were observed in all objects, although the C IV line (the primary target) was covered in the spectra of most objects. The first-epoch FOS spectra of these objects (through the G190H and G270H gratings) were collected in the early to mid 1990’s and were kindly provided, fully and uniformly reduced, by Sophia Kirhakos and Buell Jannuzi (see Schneider et al. 1993). A large fraction of them were part of the *HST* Quasar Absorption Line Key Project (hereafter, KP). Part of the reduction process was to correct the absolute wavelength scale; we have checked these corrections by comparing the observed wavelengths of securely-identified Galactic lines with their expected values and found that the agreement to be better than 0.1 \AA half of the time and never worse than 0.27 \AA . In our followup snapshot program, the quasars were observed with STIS using the G230L grating and a $52'' \times 0''.2$ slit. This grating obtains a resolution of $R \sim 1000$ and a dispersion of 1.58 \AA per pixel with two pixels per resolution element (Proffitt et al. 2002). This spectral resolution corresponds to a velocity resolution of $300\text{--}600 \text{ km s}^{-1}$ in the STIS G230L spectral range, compared to a resolution of about 230 km s^{-1} in the FOS spectra with four overlapping pixels per resolution element (Keyes et al. 1995). The spectral range for the STIS G230L is $1570\text{--}3180 \text{ \AA}$, whereas the FOS G190H and G270H spectral ranges are $1573\text{--}2330 \text{ \AA}$ and $2221\text{--}3301 \text{ \AA}$, respectively. These gratings from different instruments conveniently overlap so that a variability analysis can be conducted on the chosen objects.

To reduce the STIS data, we used the CALSTIS pipeline (Brown et al. 2002) in the Space Telescope Science Data Analysis System, within the Image Reduction and Analysis Facility (IRAF/STSDAS)¹. We did not attempt to correct the zero-point of the STIS wavelength scale, although we did determine its shift by comparing the wavelengths of Galactic lines with those of their counterparts in

¹IRAF is distributed by the National Optical Astronomy Observatories, which are operated by the Association of Universities for Research in Astronomy, Inc., under cooperative agreement with the National Science Foundation.

FOS spectra; we found that the STIS spectra were shifted by an average of 1.5 \AA (with a dispersion of 0.5 \AA). Normalized spectra were created by dividing the calibrated spectra with an *effective* continuum, which includes both the true continuum and the broad emission lines. The continuum fits were created by selecting points along the spectrum, and fitting a cubic spline to those points. We manually selected the points so that the fit would effectively interpolate across the NALs while conforming to the spectrum unaffected by the NALs. We made no effort to optimize the continuum fit at the ends of the spectra where the signal-to-noise ratio (hereafter S/N) was low. In some cases, the absorption lines are broad and/or strong enough that they irrecoverably distort the profiles of the emission lines on which they are superposed. In such cases the placement of the continuum can constitute a significant source of uncertainty in the measured EW. To include this uncertainty in our analysis, we used two extreme continuum fits, to the FOS and to the STIS spectra, in addition to the best fit. The line identification procedure and EW measurement were repeated for each of the fits. An example of two extreme continuum fits to the C IV region of the STIS spectrum of PG 1309+355 is shown in Figure 1. In Figure 2 we show the STIS spectra of all objects with the best continuum fit superposed as a solid line. The extreme continuum fits are also shown as dotted lines, but these are not readily discernible unless they differ considerably from the best fit.

After normalizing the spectra by dividing by the continuum fit, a two-step process was carried out to detect and measure absorption lines. First, the unresolved line method (Schneider et al. 1993), used in the KP project, was employed to detect lines in the spectra at the 5σ level (i.e., at 5 “significance levels” in the formalism of Schneider et al. 1993 and Jannuzi et al. 1998). On a second pass, the EWs of the identified lines were measured from the *observed* spectra by integrating the data directly. The FOS and STIS spectra were searched independently and the results were compared in the end. We measured all lines in the spectral regions of interest, irrespective of their origin. Many of the targeted doublets that were resolved in the FOS spectra were not resolved in the STIS spectra, therefore we cataloged the two members of the doublet separately in the former case and compared the sum of their EWs with the EW of the corresponding blends in the STIS spectra. Similarly, in cases where lines of interest in the STIS spectra were blended with lines from unrelated systems, we did not attempt to de-blend them but measured the total EWs of the blends and compared them with the sums of EWs of resolved lines in the FOS spectra in the end.

A significant number of lines detected in the FOS spectra were not detected in the STIS spectra, which typically had a lower S/N than the FOS spectra. In such cases, we determined and cataloged the local photon noise level and the uncertainty resulting from the placement of the continuum, which can be combined in quadrature to yield an upper limit on the EW of the line in the STIS spectrum.

The results of the measurements are listed in Table 2, where we provide the following information:

Columns 1–4: The observed wavelength and observed EW along with the uncertainty in the EW, for lines measured in the STIS spectra. The uncertainty is broken up into two parts, which should

be added in quadrature to give the final error bar on the EW: an uncertainty due to Poisson noise, σ_{ph} , and an uncertainty due to a range of possible continuum fits, σ_{cont} (discussed above and illustrated in Figure 1). In cases where the continuum fit was unambiguous, producing a negligible uncertainty in the EW, we set $\sigma_{cont} = 0$. If a line was detected in a FOS spectrum but not in the corresponding STIS spectrum, the EW column gives an upper limit, namely $W_{\lambda}^{\max}(\text{STIS}) = 5\sigma_{ph}(\text{STIS})$.

Column 5: A set of flags indicating how blended lines in the STIS spectra are compared with the corresponding resolved lines in the FOS spectra. A “ Σ ” indicates that the line listed in the STIS column is a known blend and the EW given is the total EW of the blend. In the same row, under the FOS column, we give the sum of the EWs of the individual lines making up the blend, as measured in the FOS spectrum. The rows below the total EW row in the FOS column give the EWs of the individual lines. These lines are identified with increasing index numbers in column 5. The corresponding rows in the STIS column are left blank.

Columns 6–9: The same information as in columns 1–4, but for lines measured in the FOS spectra. We note that there are only two lines detected in STIS spectra but not in FOS spectra; for these lines we provide upper limits, analogous to the STIS upper limits.

Columns 10 and 11: The difference in equivalent width between the FOS and STIS spectra: $\Delta W_{\lambda} \equiv W_{\lambda}(\text{FOS}) - W_{\lambda}(\text{STIS})$, and this difference normalized by its error bar, $\Delta W_{\lambda}/\sigma$. The error bar was computed by adding all the relevant error bars in quadrature, i.e., $\sigma^2 = \sigma_{ph}^2(\text{STIS}) + \sigma_{cont}^2(\text{STIS}) + \sigma_{ph}^2(\text{FOS}) + \sigma_{cont}^2(\text{FOS})$. In cases where a line is detected in the FOS spectrum and not in the STIS spectrum, we adopt $W_{\lambda}(\text{STIS}) = W_{\lambda}^{\max}(\text{STIS}) \equiv 5\sigma_{phot}(\text{STIS})$ and *vice versa* for a single case of a line detected with STIS but not with FOS. Entries corresponding to variable absorption lines are underlined in column 11 for easy identification.

Columns 12–15: The line identification, consisting of the ion, the rest-wavelength of the transition, the difference between the observed and expected wavelength of the line in the observer’s frame, $\Delta\lambda$, and the redshift of the absorption-line system, z_a . The redshift of the system is determined from its Ly α line, or from its strongest line, if Ly α is not available. The wavelength differences of other lines are determined as $\Delta\lambda = (1 + z_a)\lambda_{rest} - \lambda_{obs}(\text{FOS})$. In the case of blended doublets, we give identifications for the constituent lines, rather than for the doublet. Entries corresponding to variable absorption lines are underlined in column 12 for easy identification.

Column 16: The velocity offset of an absorption line for cases where this is less than 10,000 km s⁻¹. A positive velocity offset indicates a redshift of the absorption line relative to the quasar. These velocities are based on wavelengths measured from the FOS spectra whenever possible. Their uncertainties can be estimated by considering the following: (a) typical uncertainties in the absolute wavelength scales of the FOS spectra, which amount to approximately 15 km s⁻¹, (b) the fact that an uncertainty in the redshift of order $\delta z \sim 1 \times 10^{-4}$ results in an uncertainty in velocity of no more than 30 km s⁻¹, and (c) the possibility that an additional

heliocentric uncertainty of up to 30 km s^{-1} may be needed. In summary, in cases where redshift uncertainties are $\delta z \lesssim 10^{-4}$, we estimate that uncertainties in velocity offsets are of order $20\text{--}30 \text{ km s}^{-1}$, while in cases where redshifts uncertainties are $\delta z \sim 10^{-3}$, we estimate that uncertainties in velocity offsets are of order $100\text{--}200 \text{ km s}^{-1}$. Entries corresponding to variable absorption lines are underlined for easy identification.

To check our methodology, we compared the our EW measurements from the FOS spectra with those measured by Bechtold et al. (2002) from the same data and found the two sets to be in very good agreement. This comparison was facilitated by the fact that the results of Bechtold et al. (2002) are available in a convenient electronic form². We show the results of this comparison graphically in Figure 3, where we plot (a) the EW measured here against the EW measured by Bechtold et al. (2002) and (b) the distribution of *normalized* differences between our own measurements and those of Bechtold et al. (2002), namely $\Delta W_\lambda/\sigma \equiv [W_\lambda(\text{theirs}) - W_\lambda(\text{ours})]/(\sigma_{\text{theirs}}^2 + \sigma_{\text{ours}}^2)^{1/2}$. This histogram comprises 247 absorption lines, it appears symmetric about zero and contains five outliers at $|\Delta W_\lambda/\sigma| > 3$ (one is out of the range of the plot). After examining closely the outlying cases we can attribute all of them to differences in fitting the continuum.

3. Results

In the FOS spectra of the 15 quasars in our sample we have detected and identified the following absorption lines: 62 associated absorption lines (9 of which are slightly *redshifted* relative to the quasar redshift), 56 non-associated lines, and 102 Galactic lines (doublet members are counted separately in this census). If we assign the identified lines to *systems* according to their velocities, we obtain 19 associated and 12 non-associated systems (4 of the associated systems are redshifted relative to the quasar). In addition, we detected 67 unidentified lines in FOS spectra, the vast majority of which are found at wavelengths blue-ward of the Ly α emission line in the spectra of the four highest-redshift quasars in our sample. Thus, we attribute these lines to the Ly α forest and related metal-line systems.

Closely spaced lines that are resolved in FOS spectra, are sometimes blended into unresolved complexes in the STIS spectra because of the lower spectral resolution and sampling rate of the latter. Moreover, since the *S/N* of the STIS spectra is lower than that of the FOS spectra, many lines detected in the latter spectra are not detected in the former. These two effects led to us finding 39 associated and 121 non-associated lines or complexes with FOS counterparts in the STIS spectra (the complexes are identified by the flags in column 5 of Table 2). We also find one associate and one non-associated line in STIS spectra with only upper limits from FOS spectra. Moreover, for 86 lines/complexes in the FOS spectra we were only able to obtain EW upper limits from the STIS

²See <http://lithops.as.arizona.edu/~jill/QuasarSpectra/>.

spectra. Finally, we also detected 21 lines in regions of the STIS spectra not covered in the FOS spectra.

To detect NAL variability, we compared the EW difference between observations with the uncertainty resulting from photon noise and from the placement of the continuum. In particular, we computed the normalized EW difference, $\Delta W_\lambda/\sigma$, as defined in the previous section and tabulated it in column 11 of Table 2, for all lines or blended complexes detected in both the STIS and FOS spectra (in the case of blended complexes we formed the difference between the EW of the complex from STIS and the sum of EWs of constituent lines from FOS). We show the results of this comparison graphically in Figure 4, where we plot (a) the STIS and FOS EWs against each other, and (b) the distribution of the normalized EW difference. We divide the lines into two categories, for which we make separate plots: associated lines, defined by $|\Delta v| < 5,000 \text{ km s}^{-1}$ (relative to the quasar redshift; following Foltz et al. 1986), and non-associated lines (including Galactic and unidentified lines). Included in this figure are the two lines with STIS detections and FOS upper limits, bringing the total number of lines to 40 associated and 122 non-associated. It is noteworthy that out of 122 non-associated lines the difference in EW between the FOS and STIS spectra never exceeds 3σ .

The distribution of normalized EW differences in the upper panel of Figure 4b shows a number of outliers at $|\Delta W_\lambda|/\sigma > 3$, which we interpret as variable lines. We find 3 such outliers, when the expectation value, assuming a Gaussian probability distribution, is 0.11. These are the C IV $\lambda 1549$ doublets in PKS 2135–14, MRC 2251–178, and PG 2251+113 ($\Delta W_\lambda/\sigma = 3.4, 3.6, \text{ and } 5.0$, respectively). Absorption lines that are deemed to be variable are identified in Table 2 by underlining the value of $\Delta W_\lambda/\sigma$ as well as the line identification and velocity offset.

To search for additional variable lines, we compared the 5σ EW upper limits of the 86 lines not detected in the STIS spectra with the EWs of their counterparts measured from the FOS spectra. The results of this comparison are illustrated in Figure 5, where we plot the distribution of $[W_\lambda(\text{FOS}) - W_\lambda^{\text{max}}(\text{STIS})]/(\sigma_{\text{FOS}}^2 + \sigma_{\text{STIS}}^2)^{1/2}$. This is analogous to the distribution of normalized EW differences plotted in Figure 4, but with $W_\lambda(\text{STIS})$ replaced by the upper limit $W_\lambda^{\text{max}}(\text{STIS}) \equiv 5\sigma_{ph}(\text{STIS})$. The plot shows one clear outlier with a 3.3σ deviation, which is the Ly α line in PG 1718+481 at $\Delta v = +469 \text{ km s}^{-1}$, which we take as a variable line.

We have scrutinized the EW measurements of apparently variable NALs to make sure that their variability is not caused by systematic errors such as continuum placement or line blends in STIS spectra. We also compared our FOS EW values of the apparently variable lines with those of Bechtold et al. (2002) and found them to agree to “ 1σ ” or better in the cases of PG 1718+481, MRC 2251–178, and PG 2251+113. As a case in point, we note that the variability of the C IV doublet of MRC 2251–178 has already been reported and discussed by Ganguly, Charlton, & Eracleous (2001b). The analysis of this paper was carried out independently of the that paper and yielded a similar result. In the case of PKS 2135–14, our measurement differs from that of Bechtold et al. (2002), but we believe that our own measurement is the one that should be adopted. We

discuss this case in detail and present our arguments in §4.2. To provide a visual demonstration of variable lines we overlaid the normalized spectra from the FOS and STIS. Before carrying out this exercise, we convolved the FOS spectra with a Gaussian of width equal to one STIS resolution element. To account for the sampling differences between the two instruments, we discarded every other pixel in the FOS spectra to reduce the sampling rate to two pixels per resolution element. We then interpolated the FOS spectra using a cubic spline so that the final wavelength bins matched those of the corresponding STIS spectra. Finally, we aligned the wavelength scales of corresponding spectra by cross-correlating regions containing Galactic absorption lines. The results of this exercise are shown in Figure 6, where we plot segments of the original STIS and FOS spectra as well as the normalized spectra from the two instruments (after smoothing, resampling, and alignment).

4. Discussion and Conclusions

4.1. Summary of Results and Immediate Implications

We can summarize our main observational results as follows:

1. We have identified four variable associated absorption lines. None of the non-associated lines were found to vary. The EWs of the variable lines span the entire range of EWs in the absorption-line sample.
2. Each of these lines traces a different absorption *system*, implying that at least 21% (4/19) of associated systems are intrinsic.
3. The variable lines are very close to the quasar emission redshift: four out of the five have $|\Delta v| < 500 \text{ km s}^{-1}$. Moreover, one of the variable systems is redshifted relative to its host quasar.

Since not all intrinsic lines will have necessarily varied between observations, the fraction of variable systems represents a lower limit on the fraction that originate in gas in the immediate vicinity of the quasar central engine. Our result is comparable to that of Narayanan et al. (2004) who find that at 23% of the associated NALs systems that they have monitored from the ground in $z \sim 2$ quasars are variable. Moreover, Barlow et al. (1997) report a similar fraction of variable NALs ($\sim 30\%$) in higher-redshift ($z \gtrsim 2.5$) quasars. This estimate of the fraction of intrinsic NAL systems is also compatible with the estimate of 50% for $z_e \approx 2$ quasars by Ganguly et al. (1999), who used partial coverage as their diagnostic tool. We do note the caveat that the studies of Ganguly et al. (1999) and Narayanan et al. (2004) were based on a small number of objects (6 in the former and 8 in the latter), therefore their exact statistical results are somewhat uncertain.

The variability we observe could result from one of the following two processes.

1. *Fluctuations of the Quasar Light.* – Fluctuations of the quasar’s ionizing continuum induce the ionization structure of the gas to vary. One can test this hypothesis by studying the variability of lines from ions with different ionization potentials, as we discuss further below. Absorption features should have a delayed reaction to the variations of the quasar’s ionizing radiation due to the finite recombination time of the absorbing gas. In our study and in the work of Hamann et al. (1995), Aldcroft, Bechtold, & Foltz (1997), and Narayanan et al. (2004), NAL variability time scales are typically about 3–5 years in the quasar rest frame. If we take these to be upper limits to the recombination time, we can estimate a lower limit of the electron density of the absorber clouds by these time scales, following Hamann et al. (1997b). The recombination time is $\tau_{\text{rec}} \sim 1/\alpha_{\text{r}}n_{\text{e}}$, where α_{r} is the recombination rate coefficient and n_{e} is the electron density. For the C IV ion, $\alpha_{\text{r}} = 2.8 \times 10^{-12} \text{ cm}^{-3} \text{ s}^{-1}$ (Arnaud & Rothenflug 1985), which leads to $n_{\text{e}} \gtrsim 3,000 \text{ cm}^{-3}$. Using this density constraint, we can place limits on the distance of the absorber from the ionizing source. We adopt equation (3) of Narayanan et al. (2004) for the distance of the absorber from the ionizing source, which we recast as $R \approx 95 L_{44}^{1/2} n_4^{-1/2} U_{-2}^{-1/2} \text{ pc}$, where U_{-2} is the ionization parameter in units of 10^{-2} , L_{44} is the bolometric luminosity of the quasar in units of $10^{44} \text{ erg s}^{-1}$, and n_4 is the density in units of 10^4 cm^{-3} . Following Narayanan et al. (2004), we estimate the bolometric luminosity as $L_{\text{bol}} \approx 4.4\lambda L_{\lambda}$ at $\lambda = 1450 \text{ \AA}$; we obtain $L_{44} \approx 1$ for the quasars with variable C IV lines. Finally, if we assume the optimal ionization parameter, $U \approx 0.02$, from the models of Hamann et al. (1995) and use the above density constraint, we obtain $R \lesssim 100 \text{ pc}$.

2. *Bulk or Internal Motion of the Absorber.* – Bulk motion of the absorber across the quasar line of sight will cause the absorption features to vary for one or both of the following reasons: (a) a change in the column density of the absorber, and/or (b) a change in the coverage fraction in the case of a patchy absorber that covers the background source only partially. Similarly, density changes along the line of sight to the continuum source (resulting from the passage of pressure waves, for example) would have the same effect for the same reasons. The observed variability time scales could thus be equally well interpreted in this context. However, for a unique interpretation, we need more information about the location and physical conditions of the absorber. As a specific example, we consider a scenario in which the absorber is a small parcel of gas in the broad emission-line region (BELR). Assuming the continuum source is the UV-emitting region of the inner accretion disk, its size is of order $D_{\text{cont}} \sim 10 GM/c^2 = 1.5 \times 10^{14} M_8 \text{ cm}$, where M_8 is the mass of the black hole in units of $10^8 M_{\odot}$. If a parcel of gas crosses the cylinder of sight to this region at the dynamical speed of the BELR, $v_{\text{dyn}} \sim (GM/r)^{1/2} \sim 3,600 M_8^{1/2} r_{17}^{-1/2} \text{ km s}^{-1}$ (where r_{17} is the radius of the BELR in units of 10^{17} cm ; see Kaspi et al. 2000), the variability time scale will be of order 5 days. If, on the other hand, a pressure wave crosses the cylinder of sight at the speed of sound ($c_{\text{s}} \approx 10 T_4^{1/2} \text{ km s}^{-1}$, with T_4 the temperature in units of 10^4 K), the variability time scale will be of order 5 years. If we assume that the absorber is further away from the quasar central engine (e.g., in the narrow-emission line region or in the host galaxy) the above estimates can be modified accordingly.

The moral of the above discussion is that the origin of absorption-line variability can be diagnosed with the right observations. In particular, if the variability time scales are constrained to be on the order of a few months or less, internal motions (i.e., waves) in the absorber will be called into question. Such stringent constraints have, in fact, been obtained for some high-redshift quasars (see Narayanan et al. 2004, and references therein). Another test can be performed using high-dispersion spectra covering transition from a wide range of ionization states, as we discuss in detail in §4.3, below.

4.2. Discussion of Individual Objects

EX 0302–223. – The redshift quoted for this object in quasar catalogs is 1.400. This value was taken from Chanan, Downes, & Margon (1981) and is incorrect. The correct redshift is 1.409 and is reported by Margon, Downes, & Chanan (1985), who also note that the former value had a typographical error. The difference in the two redshifts translates into a velocity difference of about 1100 km s^{-1} , which would have led to a significant error in the velocities of Table 2. In fact, the absorption system at $\Delta v \approx -450 \text{ km s}^{-1}$ would have appeared at a positive velocity if the former value of the redshift were used.

QSO J0909–095. – Although the C IV doublet is detected in the FOS spectrum, the poor S/N and lower sampling of the STIS spectrum lead to a large and uninteresting upper limit to the EW at the second epoch. We do, however, detect the Ly α line in the STIS spectrum. The redshift of this object comes from a low-resolution spectrum by Knezek & Bregman (1998) in which no narrow, forbidden lines were detected. Therefore, it is unusually uncertain and is quoted only to two decimal places.

QSO 0957+561A. – A damped Ly α absorber (DLA) at $z = 1.391$ along this line of sight produces many NALs (see, for example, Dolan et al. 2000). As a result, continuum fitting is uncertain throughout the spectrum, which restricts our conclusions about the nature of the associated absorber. This object is the prototypical gravitationally-lensed quasar, discovered by Walsh, Carswell, & Weymann (1979). It is a radio-loud quasar according to its 5 GHz power ($P_{5 \text{ GHz}} = 6 \times 10^{25} \text{ W Hz}^{-1}$ based on the flux reported by Haschick et al. 1981). The redshift reported in quasar catalogs is 1.4136, which is the value measured from the broad Mg II emission line by Weymann et al. (1979b). We believe that this value does not correctly reflect the redshift of the quasar for the following reasons. There are several measurements of the redshift based on the broad C IV, C III] and Mg II UV emission lines (Walsh et al. 1979; Weymann et al. 1979b; Wills & Wills 1980; Young et al. 1981). Measurements from the same emission line by different authors agree with each other but redshifts from the C IV and C III] lines are systematically lower than the redshift from the Mg II line by about 3×10^{-3} . This is consistent with a well known trend in radio-loud quasars, in which the centroid of the broad C IV line is at the same redshift as the narrow, forbidden lines, while the the centroids of the broad Mg II and H β lines are slightly redshifted (see, for example, Brotherton et al.

1994; Marziani et al. 1996). Therefore, we believe that the redshift obtained from the C IV emission line is more likely to represent the systemic redshift of the quasar and we adopt the value of 1.4093 from Young et al. (1981). If the former redshift were adopted, the velocities listed in the last column of Table 2 would increase by 510 km s^{-1} .

PKS 2135–14. – The C IV absorption line of this object has been the subject of detailed study by several authors. It is an interesting case because the absorption lines are *redshifted* relative to the peaks of the broad emission lines and relative to the systemic redshift, as defined by the narrow, forbidden lines. In particular, Bergeron & Kunth (1983) compared *IUE* spectra taken approximately 2.6 years apart and found a 25% change in EW (from 2.0 \AA in 1979 to 2.5 \AA in 1981) as well as a shift of the absorption-line centroid by 300 km s^{-1} between the two epochs. We find a significant change in EW between the STIS and FOS observations (from 4.7 \AA in 1992 to 3.2 \AA in 2000; see illustration in Fig. 6), as well as a significant change between the *HST* (1992 and 2000) and *IUE* (1979 and 1981) observations. However, the EW we measure from the FOS spectrum is higher than the values measured by Bechtold et al. (2002) and Hamann et al. (1997c) (4.7 \AA by us *vs* 3.1 \AA and 3.6 \AA by them). The difference is a result of the placement of the *effective* continuum (i.e., the emission line profile). We have experimented with several different fits to the peak and blue side of the C IV emission-line profile including using the profile of the C III] $\lambda 1909$ line as a template. In Figure 7 we show the C IV profile of this object as observed with the FOS, with our two extreme continuum fits superposed as smooth, solid lines. The fit based on the C III] profile falls between the two extremes and is the one we adopt as the optimal. We obtained the EW by integrating the normalized spectrum directly between the two extreme points where the fitted profile meets the observed profile. In contrast, the fit used by Hamann et al. (1997c) resembles the shape of our lowest acceptable fit but is placed somewhat lower (see their Fig. 3); it suffers from the drawback that the resulting peak of the C IV line falls a few Ångstrom short-ward of its nominal wavelength. Those authors obtained the EW by fitting the absorption profile with 2 or 4 components. The fit used by Bechtold et al. (2002) was a simple interpolation over the primary absorption trough (illustrated schematically as a dotted line in Fig. 7), which also led to a low value for the EW. Bergeron & Boissé (1986) and Hamann et al. (1997c) have studied the ionization conditions in this particular absorption system and concluded that the ionization parameter is likely to be high ($U \approx 0.25$), although lower values (as low as $U \approx 3 \times 10^{-3}$) could not be ruled out. They discussed a number of possible scenarios for the absorber, including galaxies within the cluster harboring the quasar, the quasar host galaxy itself, and gas intrinsic to the quasar central engine, but they were not able to select one of these scenarios as an obvious favorite. The variability results we present here, especially when combined with the earlier results of Bergeron & Kunth (1983), make a strong case that this absorber is intrinsic to the quasar central engine. This finding is particularly interesting in view of the fact that this absorption-line system appears to be redshifted relative to the quasar. Such a redshift does not necessarily imply infall of the absorbing gas toward the quasar central engine because other scenarios can be found that produce such a redshifted absorption line.

For example, a parcel of gas in a rotating accretion-disk wind passing in front of an *extended* continuum source at the center of the disk can easily produce a redshifted absorption line.

4.3. Future Prospects

The variability of lines from ions of different ionization potentials can be used to distinguish between variations in the ionizing continuum and variations of the column density (due to transverse motion of the absorber). Ideally, high-resolution ($R \gtrsim 40,000$) spectra should be used for such a test so that the absorption lines are fully resolved. Under these conditions one can determine whether the background source is partially covered and infer the column density of the absorber, thus constraining its location (see, for example Barlow & Sargent 1997; Hamann et al. 1997a; Ganguly et al. 1999).

To illustrate and evaluate the method, we carried out the following exercise. We used the photoionization code CLOUDY (Ferland 1996) to simulate the the ionization structure of the absorber, assuming that the incident ionizing spectrum is that of Mathews & Ferland (1987). Input parameters for the models are the total hydrogen density, the ionization parameter, and the total hydrogen column density for each component, assuming Solar abundances and a metallicity of 1/3 the Solar value. Throughout this exercise we assumed that the coverage fraction is unity for all transitions and that it did not change as the column density or ionization parameter changed. The results for simulated profiles are not sensitive to the hydrogen density in the optically thin regime; values from 10^5 to 10^9 cm^{-3} give similar results. For our particular example we have assumed that the absorber consists of three kinematic “components” at relative velocities -75 , 0 , and 20 km s^{-1} , with column densities of $\log N_{\text{H}} = 19.5$, 20 , and 19 , and broadening parameters $b = 8$, 12 , and 10 km s^{-1} . The ionization parameter is taken to be $\log U = -2$. In Figure 8 we display the synthetic spectra resulting from this exercise. The middle set of panels show a simulated spectrum ($R = 23,500$; $S/N = 20$) of the C IV profile along with a variety of other transitions. The left-hand set of panels of Figure 8 demonstrate the effect of bulk motion, which we represent as a decrease of the column density of each absorption component by an order of magnitude. The result is that all of the absorption lines become weaker, regardless of ionization state. The right-hand set of panels demonstrates the effect of increasing the continuum strength and hence the ionization parameter by an order of magnitude. The lines from the lower ionization species are not detected, while the lines from the higher ionization species, such as N V and O VI become stronger. A decrease in the total column density and an increase in the continuum strength have a similar effect on the C IV profile, but the difference between the two scenarios can be diagnosed if multiple transitions from a variety of ionization states are observed.

With the above scientific questions and technical considerations in mind, the next logical step in our systematic study of intrinsic NALs is to target specific quasars whose NALs are demonstrably intrinsic. If the quasars cooperate, we can infer the physical conditions and location of the absorber through repeated observations. Thus we will be able to assess the role of the NAL gas in the overall

accretion flow. Alternatively, significant progress can also be made by single epoch observations of intrinsic (and other, associated) NALs at high spectral resolution. Using high-resolution spectra that encompass transitions from a wide range of ionization states, we can determine the ionization structure of the absorber and constrain its distance from the ionizing source.

This work was supported by grant HST-GO-08681.01-A from the Space Telescope Science Institute, which is operated by the Association of Universities for Research in Astronomy, Inc., under NASA contract NAS5-26555. We also acknowledge support from NASA grant NAG5-10817. We have made use of the NASA/IPAC Extragalactic Database (NED) which is operated by the Jet Propulsion Laboratory, California Institute of Technology, under contract with the NASA. We thank the anonymous referee for many valuable technical comments. We are grateful to Sofia Kirhakos and Buell Jannuzi for providing us with the uniformly and fully reduced spectra of quasars observed by the *HST*/FOS. We also thank Fred Hamann for useful discussions and especially for reminding us of the importance of accurate redshifts.

REFERENCES

- Aldcroft, T. L., Bechtold, J., & Elvis, M. 1994, *ApJS*, 93, 1
- Aldcroft, T., Bechtold, J., & Foltz, C. 1997, in *Mass Ejection from Active Galactic Nuclei*, eds. N. Arav & R. J. Weymann, *ASP Conf. Ser.* 128 (San Francisco: ASP), 25
- Anderson, S. F., Weymann, R. J., Foltz, C. B., & Chaffee, F. H., Jr. 1987, *AJ*, 94, 278
- Arnaud, M. & Rothenflug, R. 1985, *A&AS*, 60, 425
- Bahcall, J. N. 1993, *ApJS*, 87, 1
- Barlow, T. A. 1993, Ph.D. Thesis, University of California, San Diego
- Barlow, T. A. 1995, *BAAS*, 27, 872
- Barlow, T. A. & Sargent, W. L. W. 1997, *AJ*, 113, 136
- Barlow, T. A., Hamann, F., & Sargent, W. L. W. 1997, in *Mass Ejection from Active Galactic Nuclei*, eds. N. Arav & R. J. Weymann, *ASP Conf. Ser.* 128 (San Francisco: ASP), 13
- Bechtold, J., Dobrzycki, A., Wilden, B., Morita, M., Scott, J., Dobrzycka, D., Tran, K.-V., & Aldcroft, T. L. 2002, *ApJS*, 140, 143
- Bergeron, J., & Boissé, P. 1986, *â*, 168, 6
- Bergeron, J., & Kunth, D. 1983, *MNRAS*, 205, 1053
- Bergeron, J., Boksenberg, A., Dennefeld, M., & Tarengi, M. 1983, *MNRAS*, 202, 125

- Boroson, T. A. & Green, R. F. 1992, *ApJS*, 80, 109
- Boissé, P., Le Brun, V., Bergeron, J., & Deharveng, J.-M. 1998, *A&A*, 333, 841
- Brandt, W. N., Laor, W., & Wills, B. J. 2000, *ApJ*, 528, 637
- Brotherton, M. S., Wills, B. J., Steidel, C. C., & Sargent, W. L. W. 1994, *ApJ*, 423, 131
- Brown, T., et al. 2002, in *HST STIS Data Handbook*, Version 4.0, ed. B. Mobasher (Baltimore: STScI)
- Chanan, G. A., Downes, R. A., & Margon, B. 1981, *ApJ*, 243, L5
- Dolan, J. F., Michalitsianos, A. G., Nguyen, Q. T., & Hill, R. J. 2000, *ApJ*, 539, 111
- Eracleous, M. & Halpern, J. P. 2004, *ApJS*, 150, in press
- Foltz, C. B., Weymann, R. J., Peterson, B. M., Sun, L., Malkan, M. A. & Chaffee, F. H., Jr. 1986, *ApJ*, 307, 504
- Ferland, G. 1996, *Hazy*, University of Kentucky Internal Report
- Ganguly, R., Eracleous, M., Charlton, J. C., & Churchill, C. W. 1999, *AJ*, 117, 2594
- Ganguly, R., Bond, N. A., Charlton, J. C., Eracleous, M., Brandt, W. N., & Churchill, C. W. 2001a, *ApJ*, 549, 123
- Ganguly, R., Charlton, J. C., & Eracleous, M. 2001b, *ApJ*, 556, L7
- Hamann, F., Barlow, T. A., Beaver, E. A., Burbidge, E. M., Cohen, R. D. Junkkarinen, V. & Lyons, R. 1995, *ApJ*, 443, 606
- Hamann, F., Barlow, T. A., Junkkarinen, V. & Burbidge, E. M. 1997a, *ApJ*, 478, 80
- Hamann, F., Barlow, T. A., & Junkkarinen, V. 1997b, *ApJ* 487, 87
- Hamann, F., Beaver, E. A., Cohen, R., Junkkarinen, V., Lyons, R. W., & Burbidge, E. M. 1997c, *ApJ*, 488, 155
- Hamann, F. & Sabra, B. 2004, in *AGN Physics with the Sloan Digital Sky Survey*, eds. G. T. Richards & P. B. Hall (San Francisco: ASP), in press (astro-ph/0310668).
- Haschick, A. D., Moran, J. M., Reid, M. J., Davis, M., & Lilley, A. E., *ApJ*, 243, L57.
- Mathews, W. G. & Ferland, G. J. 1987, *ApJ*, 323, 456
- Jannuzi, B. 2002, in *Extragalactic Gas at Low Redshift*, eds. J. S. Mulchaey & J. T. Stocke, ASP Conf. Ser. 254 (San Francisco: ASP), 13

- Jannuzi, B. et al. 1998, ApJS, 118, 1
- Kaspi, S., Smith, P. S., Netzer, H., Maoz, D., Jannuzi, B. T., & Giveon, U. 2000, ApJ, 533, 631
- Keyes, C. D., et al. 1995, FOS Instrument Handbook, Version 6.0 (Baltimore: STScI)
- Knezek, P. M. & Bregman, J. N. 1998, AJ, 115, 1737
- Le Brun V., Bergeron J., Boissé P., & Deharveng J. M. 1997, A&A, 321, 733
- Margon, B., Downes, R. A., & Chanan, G. A. 1985, ApJS, 59, 23
- Marziani, P., Sulentic, J. W., Dultzin-Hacyan, D., Calvani, M., & Moles, M. 1996, ApJS, 104, 37
- Murray, N., Chiang, J., Grossman, S. A., & Voit, G. M. 1995 ApJ, 451, 498
- Narayanan, D., Hamann, F., Barlow, T., Burbidge, E. M., Cohen, R. D., Junkkarinen, V., & Lyons, R. 2004, ApJ, in press (astro-ph/0301668)
- Netzer, H., Brotherton, M. S., Wills, B. J., Han, M., Wills, D., Baldwin, J. A., Ferland, G. J., & Browne, I. W. A. 1995, ApJ, 448, 27
- Proffitt, C., et al. 2002, STIS Instrument Handbook, Version 6.0 (Baltimore: STScI)
- Proga, D., Stone, J. M., & Kallman, T. R. 2000, ApJ, 543, 686
- Richards, G. T., York, D. G., Yanny, B., Kollgaard, R. I., Laurent-Muehleisen, S. A., & Vanden Berk, D. E. 1999, ApJ, 513, 576
- Schmidt, M. & Green, R. F. 1983, ApJ, 269, 352
- Schneider, D. P., et al. 1993 ApJS, 87, 45
- Turnshek, D. A. 1987, in QSO Absorption Lines: Probing the Universe ed. J. C. Blades, D. A. Turnshek, & C. Norman (Cambridge: Cambridge Univ. Press), 17
- Turnshek, D. A., Foltz, C. B., Grillmair, C. J., & Weymann, R. J. 1988, ApJ, 325, 651
- Walsh, D., Carswell, R. F., & Weymann R. J. 1979, Nature, 279, 381
- Wampler, E. J., Bergeron, J., & Petitjean, P. 1993, A&A, 273, 15
- Weymann, R. J., Williams, R. E., Peterson, B. M., & Turnshek, D. A. 1979, ApJ, 234, 33
- Weymann, R. J., Chaffee, F. H., Davis, M., Carleton, N. P., & Carswell, R. F. 1979, ApJ, 233, L43
- Weymann, R. J., Morris, S. L., Foltz, C. B., & Hewett, P. C. 1991, ApJ, 373, 23
- Wills, D. & Wills, B. J. 1976, ApJS, 31, 143

Wills, D. & Wills, B. J. 1980, ApJ, 238, 1

Wills, B. J., Laor, A., Brotherton, M. S., Wills, D., Wilkes, B. J., Ferland, G. J., & Shang, Z. 1999, ApJ, 515, L53

Young, P., Sargent, W. L. W., Boksenberg, A., & Oke, J. B. 1981, ApJ, 249, 415

Table 1. Journal of Observations

Object	z^a	Targeted Lines	Obs. Date (UT mm/dd/yyyy)		Interval (years)	z Refs ^b	Pub Refs ^c
			FOS	STIS			
EX 0302–223	1.409	N v, Ly α , O vi	12/07/1995	02/22/2001	5.22	1	1
QSO J0909–095	0.63	C iv	10/29/1996	03/04/2001	4.35	2	none
PG 0953+414	0.2341(4)	C iv	11/05/1991 ^d 06/18/1991 ^d	01/21/2001	9.22 9.60	3	2,3
QSO 0957+561A	1.4093(1)	N v, Ly α , O vi	01/26/1995	09/08/2000	5.62	4	4
MRC 1118+128	0.685(1)	C iv, Ly α	02/26/1995	03/28/2001	6.09	5	none
PG 1241+176	1.273	O vi, Ly α	12/08/1992	03/19/2001	8.28	6	2
PG 1309+355	0.184	C iv	05/20/1996	04/04/2001	4.88	6,7	5
PG 1351+640	0.0882(2)	C iv	09/05/1991	05/03/2001	9.67	3	5,6
PG 1411+442	0.0896(5)	C iv	10/03/1992	02/12/2001	8.37	3	2
PG 1425+260	0.366	C iv, N v	06/29/1996	04/26/2001	4.83	6,7	5
3C 351	0.37194(4)	C iv	10/22/1991	08/18/2001	9.83	8	2,7
PG 1718+481	1.084	N v, Ly α , O vi	05/13/1993	03/09/2001	7.82	7	2
PKS 2135–14	0.20036(4)	C iv	09/13/1992	09/20/2000	8.02	9,10	8
MR 2251–178	0.06398(6)	C iv	08/02/1996	11/05/2000	4.26	11	9
PG 2251+113	0.3255(3)	C iv	12/04/1992	05/01/2001	8.41	3	7,10

^aSee §2 and §4.2 of the text for a discussion of the adopted emission redshift values and related velocity uncertainties. The figure in parenthesis gives the uncertainty in the last digit whenever this is available.

^b*References to adopted redshift measurements.* – (1) Margon, Downes, & Chanan (1985); (2) Knezek & Bregman (1998); (3) Marziani et al. (1996); (4) Young et al. (1981); (5) Wills & Wills (1976); (6) Schmidt & Green (1983); (7) Boroson & Green (1992); (8) Eracleous & Halpern (2004); (9) Hamann et al. (1997c); (10) Bergeron & Boissé (1986); (11) Bergeron et al. (1983).

^c*References to previously published FOS spectra.* – (1) Boissé et al. (1998); (2) Jannuzi et al. (1998); (3) Wills et al. (1999); (4) Dolan et al. (2000); (5) Brandt, Laor, & Wills (2000, the spectra were discussed but not displayed); (6) Marziani et al. (1996); (7) Bahcall et al. (1993); (8) Hamann et al. (1997c); (9) Ganguly et al. (2001b); (10) Netzer et al. (1995).

^dThe earlier date corresponds to the FOS G190H spectrum and the later date the FOS G270H spectrum.

Table 2. Line Identifications and Equivalent Width Measurements

STIS				Blend	FOS				ΔW_λ	$\frac{\Delta W_\lambda}{\sigma}$	Line ID				
λ_{obs}	W_λ	σ_{ph}	σ_{cont}		λ_{obs}	W_λ	σ_{ph}	σ_{cont}			Ion	λ_{rest}	$\Delta\lambda$	z_{abs}	Δv
(Å)	(Å)	(Å)	(Å)	Flag	(Å)	(Å)	(Å)	(Å)	(Å)	(11)	(12)	(Å)	(Å)	(15)	(km s ⁻¹)
(1)	(2)	(3)	(4)	(5)	(6)	(7)	(8)	(9)	(10)	(11)	(12)	(13)	(14)	(15)	(16)
EX 0302–223 ($z_e = 1.409$)															
2158.66	0.84	0.22	0.84			out of range		
2169.36	1.07	0.23	1.07			out of range		
2185.40	1.83	0.32	1.83			out of range			H I	937.80	2.14	1.32806	–9945
2202.38	1.58	0.26	1.58			out of range		
2212.46	2.39	0.27	2.39			out of range			H I	949.74	1.40	1.32806	–10048
2254.02	1.50	0.23	0.05		2253.75	1.48	0.10	0.00	–0.01	–0.06	H I	937.80	–1.88	1.40523	–719
2266.48	2.45	0.22	0.17		2264.09	2.83	0.09	0.00	0.38	1.32	H I	972.54	–0.03	1.32806	–10224
2278.26	2.38	0.27	0.09		2279.34	2.24	0.12	0.01	–0.13	–0.44	Si II	1193.29	–0.81	0.91081	...
2300.17	2.28	0.28	0.05	Σ	2298.62	1.30	0.11	0.13	–0.98	–2.98
...	1	2296.67	0.86	0.08	0.00
...	2	2300.55	0.44	0.07	0.13
2305.36	1.16	0.28	1.16	Σ	2305.86	1.28	0.08	0.71	0.11	0.08
...	1	1132.05	0.71	0.05	0.71
...	2	2305.86	0.57	0.07	0.00	Si III	1206.50	0.47	0.91081	...
2325.04	2.62	0.27	0.10	Σ	2326.19	2.90	0.12	0.12	0.28	0.83
...	1	2323.08	1.70	0.09	0.12	H I	1215.67	0.17	0.91081	...
...	2	2329.58	1.20	0.08	0.00
2344.63	<0.90	0.18	0.15		2344.03	0.32	0.06	0.02	> –0.58	> –2.39	Fe II	2344.21	–0.18	0	...
2373.46	1.28	0.20	0.17		2372.33	1.66	0.08	0.04	0.38	1.35	Fe II	2374.46	–2.13	0	...
2383.34	<0.95	0.19	0.16		2382.77	0.31	0.06	0.02	> –0.64	> –2.50	Fe II	2382.76	0.01	0	...
2391.21	6.57	0.27	0.16	Σ	2390.16	6.86	0.16	0.48	0.29	0.48
...	1	2380.53	0.34	0.06	0.34	Fe II	2382.76	–2.23	0	...
...	2	2390.08	5.70	0.13	0.34	H I	1025.72	2.14	1.32806	–9970
2397.27	<1.05	0.21	0.08		2397.52	0.81	0.07	0.02	> –0.24	> –1.02	Si II	1193.29	–0.02	1.00916	...
2414.48	2.13	0.21	0.05		2414.85	1.77	0.09	0.11	–0.36	–1.39
2428.08	1.59	0.20	1.59		2424.60	1.10	0.07	1.10	–0.49	–0.25	Si III	1206.50	0.55	1.00916	...

Table 2—Continued

STIS				Blend	FOS				ΔW_λ	$\frac{\Delta W_\lambda}{\sigma}$	Line ID				
λ_{obs}	W_λ	σ_{ph}	σ_{cont}		λ_{obs}	W_λ	σ_{ph}	σ_{cont}			Ion	λ_{rest}	$\Delta\lambda$	z_{abs}	Δv
(Å)	(Å)	(Å)	(Å)	Flag	(Å)	(Å)	(Å)	(Å)	(Å)	(11)	(12)	(Å)	(Å)	(15)	(km s ⁻¹)
(1)	(2)	(3)	(4)	(5)	(6)	(7)	(8)	(9)	(10)	(11)	(12)	(13)	(14)	(15)	(16)
2444.69	15.55	0.25	0.76		2442.47	15.04	0.14	0.30	-0.51	-0.59	H I	1215.67	0.00	1.00916	...
2469.60	0.92	0.15	0.03		2467.50	1.14	0.06	0.00	0.22	1.33	H I	1025.72	0.41	1.40523	-420
2490.06	1.97	0.21	0.11	Σ	2485.41	2.31	0.11	0.24	0.34	0.94
...	1	2482.32	0.94	0.06	0.00	O VI	1031.93	0.30	1.40523	-434
...	2	2488.94	1.37	0.10	0.24	N V	1238.82	-0.04	1.00916	...
2496.38	<0.85	0.17	0.28		2495.73	0.38	0.06	0.05	> -0.47	> -1.40	O VI	1037.62	0.02	1.40523	-468
2501.81	1.19	0.19	0.37		2499.92	0.89	0.07	0.00	-0.30	-0.71	N V	1242.80	2.93	1.00916	...
2517.27	0.51	0.19	0.51		2513.89	0.29	0.05	0.29	-0.22	-0.35
2526.34	0.38	0.16	0.38		2532.45	0.77	0.07	0.77	0.39	0.45	Si II	1260.42	0.07	1.00916	...
2534.46	1.64	0.23	0.78		2532.45	1.55	0.07	0.00	-0.10	-0.12	Si II	1260.42	0.07	1.00916	...
2560.39	1.90	0.25	0.13	Σ	2556.29	1.61	0.13	0.32	-0.29	-0.66
...	1	2551.07	0.28	0.07	0.28	C II	1334.53	1.04	0.91081	...
...	2	2558.63	1.33	0.11	0.15
2575.38	<0.90	0.18	0.10		2576.11	0.57	0.07	0.31	> -0.33	> -0.87
2600.17	<0.90	0.18	0.09		2600.61	0.56	0.06	0.25	> -0.34	> -1.04	Fe II	2600.17	0.44	0	...
2621.83	1.61	0.21	0.01	Σ	2616.62	1.61	0.09	0.51	0.01	0.02
...	1	2612.56	0.39	0.05	0.00
...	2	2616.17	0.71	0.05	0.00	O I	1302.17	-0.09	1.00916	...
...	3	2621.13	0.51	0.06	0.51	Fe II	2344.21	0.16	0.11806	...
2629.48	0.70	0.17	0.00		2628.56	0.53	0.05	0.01	-0.17	-0.96
2654.41	<0.95	0.19	0.03		2654.45	0.33	0.05	0.02	> -0.62	> -3.10	Fe II	2374.46	-0.34	0.11806	...
2670.85	2.60	0.25	0.05		2668.96	2.01	0.06	0.03	-0.59	-2.23	C I	1328.83	-0.87	1.00916	...
2683.98	1.58	0.20	0.05		2681.72	1.57	0.08	0.03	-0.00	-0.02	C II	1334.53	0.44	1.00916	...
2690.21	0.70	0.21	0.70		2689.94	0.26	0.06	0.26	-0.44	-0.57
2708.85	0.57	0.22	0.57		2709.38	0.17	0.06	0.17	-0.40	-0.63
2734.63	1.18	0.21	0.34		2732.62	0.78	0.05	0.02	-0.40	-1.00
2750.37	0.46	0.19	0.46		2748.26	0.00	0.00	0.00	0.46	0.92

Table 2—Continued

STIS				Blend	FOS				ΔW_λ	$\frac{\Delta W_\lambda}{\sigma}$	Line ID				
λ_{obs}	W_λ	σ_{ph}	σ_{cont}		λ_{obs}	W_λ	σ_{ph}	σ_{cont}			Ion	λ_{rest}	$\Delta\lambda$	z_{abs}	Δv
(Å)	(Å)	(Å)	(Å)	Flag	(Å)	(Å)	(Å)	(Å)	(Å)	(11)	(12)	(Å)	(Å)	(15)	(km s ⁻¹)
(1)	(2)	(3)	(4)	(5)	(6)	(7)	(8)	(9)	(10)	(11)	(12)	(13)	(14)	(15)	(16)
2763.19	2.12	0.20	0.03		2761.03	2.09	0.06	0.00	-0.02	-0.10
2770.67	<0.90	0.18	0.02		2770.22	0.28	0.05	0.00	> -0.62	> -3.30
2797.03	<0.95	0.19	0.03		2796.40	0.71	0.05	0.11	> -0.24	> -1.06	Mg II	2796.35	0.05	0	...
2803.11	2.41	0.22	0.03		2800.62	2.60	0.05	0.24	0.19	0.57	Si IV ^b	1393.76	0.35	1.00916	...
2810.73	0.73	0.16	0.10		2809.76	0.91	0.07	0.11	0.18	0.78	Si III	1206.50	0.96	1.32806	-10137
2818.74	<0.90	0.19	0.11		2818.76	1.08	0.05	0.04	>0.18	>0.79	Si IV	1402.77	0.37	1.00916	...
2832.35	5.39	0.20	0.13		2830.15	5.99	0.06	0.03	0.61	2.40	H I	1215.67	-0.00	1.32806	-10239
2855.35	0.73	0.17	0.08		2853.45	0.64	0.04	0.00	-0.09	-0.44	Mg I	2852.96	0.49	0	...
2868.37	<0.80	0.16	0.04		2868.17	0.67	0.05	0.00	> -0.13	> -0.75
2876.12	<0.75	0.15	0.02		2875.98	0.41	0.04	0.00	> -0.34	> -2.17
2882.33	<0.75	0.15	0.01		2882.32	0.40	0.05	0.00	> -0.35	> -2.21
2885.43	<0.75	0.15	0.01		2884.78	0.18	0.04	0.00	> -0.57	> -3.66
2890.08	<0.75	0.15	0.02		2890.76	0.29	0.04	0.00	> -0.46	> -2.94
2907.32	0.86	0.12	0.06		2907.04	1.13	0.05	0.00	0.27	1.89	Fe II	2600.17	-0.11	0.11806	...
2916.45	<0.65	0.13	0.04		2916.97	0.19	0.03	0.00	> -0.46	> -3.30	Si II	1526.71	-0.28	0.91081	...
2925.84	1.06	0.15	0.04		2923.96	0.85	0.04	0.00	-0.21	-1.31	H I	1215.67	0.00	1.40523	-470
2937.23	1.14	0.18	0.19		2936.47	0.65	0.05	0.03	-0.49	-1.88	Si II	1260.42	2.13	1.32806	-10021
2961.52	1.31	0.20	0.05	Σ	2960.59	1.81	0.09	0.17	0.51	1.80
...	1	2958.30	0.96	0.05	0.02	C IV	1548.19	0.00	0.91081	...
...	2	2962.55	0.86	0.08	0.17	C IV	1550.77	-0.67	0.91081	...
2979.44	<0.55	0.11	0.15		2979.44	0.43	0.07	0.05	> -0.12	> -0.59	N V	1238.82	0.21	1.40523	-490
2989.96	<0.55	0.11	0.13		2989.96	0.26	0.05	0.03	> -0.29	> -1.61	N V	1242.81	-0.72	1.40523	-398
3067.99	1.40	0.28	0.01		3066.81	0.91	0.06	0.02	-0.49	-1.74	Si II	1526.71	-0.58	1.00916	...
3112.29	5.43	0.47	0.15	Σ	3111.43	5.77	0.18	0.73	0.34	0.38
...	1	3106.18	0.57	0.05	0.02
...	2	3111.48	3.26	0.16	0.73	C IV	1548.19	0.92	1.00916	...
...	3	3116.90	1.94	0.06	0.11	C IV	1550.77	1.16	1.00916	...

Table 2—Continued

STIS				Blend Flag	FOS				ΔW_λ (Å)	$\frac{\Delta W_\lambda}{\sigma}$ (11)	Line ID				
λ_{obs} (Å) (1)	W_λ (Å) (2)	σ_{ph} (Å) (3)	σ_{cont} (Å) (4)		λ_{obs} (Å) (6)	W_λ (Å) (7)	σ_{ph} (Å) (8)	σ_{cont} (Å) (9)			Ion (12)	λ_{rest} (Å) (13)	$\Delta\lambda$ (Å) (14)	z_{abs} (15)	Δv (km s ⁻¹) (16)
3125.96	<1.95	0.39	0.10		3125.86	0.83	0.05	0.16	> -1.12	> -2.57	Mg II	2796.35	-0.63	0.11806	...
3133.73	<1.85	0.37	0.12		3133.69	0.91	0.06	0.20	> -0.94	> -2.13	Mg II	2803.53	-0.82	0.11806	...
QSO J0909-095 ($z_e = 0.63$)															
1982.52	24.26	0.79	0.00		out of range				H I	1215.67	0.00	0.6308	+148
2344.15	<3.05	0.61	0.00		2344.38	1.01	0.11	0.00	> -2.04	> -3.29	Fe II	2344.21	0.17	0	...
2373.56	<2.65	0.53	0.00		2374.24	0.96	0.11	0.00	> -1.69	> -3.12	Fe II	2374.46	-0.22	0	...
2382.85	<2.55	0.51	0.00		2382.92	1.42	0.13	0.00	> -1.13	> -2.15	Fe II	2382.77	0.15	0	...
2523.78	<1.20	0.24	0.00		2523.71	0.62	0.05	0.00	> -0.58	> -2.37	C IV	1548.19	-1.08	0.6308	+26
2528.43	<1.30	0.26	0.00		2527.99	0.55	0.05	0.00	> -0.75	> -2.83	C IV	1550.77	-1.01	0.6308	+38
2587.30	<2.00	0.40	0.00		2586.76	0.76	0.08	0.00	> -1.24	> -3.04	Fe II	2586.50	0.05	0	...
2599.69	<2.20	0.44	0.00		2599.74	0.83	0.08	0.00	> -1.37	> -3.06	Fe II	2600.17	0.05	0	...
2796.56	<2.75	0.55	0.00		2796.43	1.37	0.10	0.00	> -1.38	> -2.47	Mg II	2796.35	0.05	0	...
2804.31	<4.10	0.82	0.00		2803.79	1.24	0.08	0.00	> -2.86	> -3.47	Mg II	2803.53	0.05	0	...
PG 0953+414 ($z_e = 0.2341$)															
1671.01	<1.70	0.34	0.00		1670.76	0.56	0.11	0.00	> -1.14	> -3.19	Al II	1670.79	-0.03	0	...
1710.12	1.04	0.24	0.00		1710.12	< -0.40	0.08	0.00	0.64	< -2.53	Si IV	1398.26 ^a	0.00	0.2230	-2699
2345.48	2.28	0.12	1.10		2344.50	1.69	0.13	0.64	0.59	0.46	Fe II	2344.21	0.49	0	...
2374.52	<0.50	0.10	0.00		2374.46	0.37	0.07	0.00	> -0.13	> -1.07	Fe II	2374.46	0.00	0	...
2383.71	0.82	0.13	0.00		2382.92	0.85	0.09	0.00	0.03	0.19	Fe II	2382.76	0.16	0	...
2587.96	0.57	0.12	0.11		2586.59	0.81	0.08	0.00	0.23	1.25	Fe II	2586.65	-0.06	0	...
2601.33	0.84	0.13	0.14		2599.79	0.88	0.08	0.05	0.04	0.21	Fe II	2600.17	-0.38	0	...
2797.55	1.76	0.13	0.17		2796.19	1.36	0.08	0.02	-0.40	-1.76	Mg II	2796.35	-0.16	0	...
2803.09	1.11	0.12	0.05		2803.64	1.33	0.09	0.12	0.22	1.11	Mg II	2803.53	0.11	0	...
2853.19	0.63	0.13	0.00		2852.79	0.57	0.06	0.06	-0.06	-0.41	Mg I	2852.96	-0.17	0	...
QSO 0957+561A ($z_e = 1.4093$)															
2191.16	1.30	16.09	1.01		out of range			
2206.43	1.22	0.26	0.00		out of range			

Table 2—Continued

STIS				Blend	FOS				ΔW_λ	$\frac{\Delta W_\lambda}{\sigma}$	Line ID				
λ_{obs}	W_λ	σ_{ph}	σ_{cont}		λ_{obs}	W_λ	σ_{ph}	σ_{cont}			Ion	λ_{rest}	$\Delta\lambda$	z_{abs}	Δv
(Å)	(Å)	(Å)	(Å)	Flag	(Å)	(Å)	(Å)	(Å)	(Å)	(11)	(12)	(Å)	(Å)	(15)	(km s ⁻¹)
(1)	(2)	(3)	(4)	(5)	(6)	(7)	(8)	(9)	(10)	(11)	(12)	(13)	(14)	(15)	(16)
2215.89	0.98	0.22	0.00						H I	926.23	0.00	1.39238	-2113
2225.89	2.22	0.20	0.00		2226.08	2.36	0.10	0.00	0.14	0.65	H I	930.75	-0.63	1.39238	-2197
2242.12	3.38	0.22	0.02		2242.65	3.45	0.08	0.00	0.08	0.32	H I	937.80	-0.94	1.39238	-2236
2271.28	4.93	0.25	0.05	Σ	2274.16	4.75	0.11	0.12	-0.18	-0.60
...	1	2271.11	4.02	0.09	0.12	H I	949.74	-1.04	1.39238	-2248
...	2	2277.23	0.73	0.06	0.00
2312.43	2.51	0.25	0.37	Σ	2311.55	3.30	0.13	0.40	0.79	1.29
...	1	2308.23	1.62	0.07	0.00
...	2	2314.30	1.68	0.11	0.40
2325.65	3.70	0.21	0.41		2325.38	3.95	0.06	0.25	0.25	0.53	H I	972.54	-1.30	1.39238	-2280
2336.65	4.51	0.25	0.29	Σ	2340.51	4.78	0.11	0.25	0.27	0.58
...	1	2336.38	3.15	0.08	0.24	C III	977.02	-1.03	1.39238	-2243
...	2	2341.02	0.87	0.04	0.05
...	3	2344.17	0.76	0.05	0.04	Fe II	2344.21	-0.04	0	...
2352.07	<1.00	0.20	0.10		2351.78	1.03	0.06	0.00	>0.03	>0.13
2365.94	2.64	0.20	0.14		2364.20	3.56	0.07	0.45	0.92	1.78	O I	988.65	-1.04	1.39238	-2242
2375.29	<0.95	0.19	0.22		2374.93	0.75	0.05	0.13	>-0.20	>-0.62	Fe II	2374.46	0.47	0	...
2381.93	0.94	0.25	0.94		2382.91	0.63	0.05	0.63	-0.31	-0.26	Fe II	2382.76	0.15	0	...
2413.48	0.77	0.18	0.05		2412.18	0.86	0.06	0.07	0.09	0.41	N I	1134.98	-0.06	1.12536	...
2423.06	1.65	0.23	0.02		2424.76	1.94	0.07	0.34	0.29	0.70
2453.70	4.86	0.23	0.34		2452.55	4.91	0.06	0.18	0.06	0.13	H I	1025.72	-1.37	1.39238	-2279
2468.24	0.89	0.16	0.12		2467.78	1.19	0.05	0.02	0.30	1.43	O VI	1031.93	-0.99	1.39238	-2232
2480.24	3.78	0.23	0.38	Σ	2484.18	4.36	0.09	0.30	0.58	1.06
...	1	2478.49	2.30	0.07	0.22	C II	1036.34	-0.83	1.39238	-2212
...	2	2485.08	0.93	0.03	0.14	O VI	1037.62	2.70	1.39238	-1786
...	3	2489.20	1.13	0.04	0.15
2519.77	0.76	0.15	0.05		2519.23	1.24	0.05	0.02	0.48	2.87

Table 2—Continued

STIS				Blend	FOS				ΔW_λ	$\frac{\Delta W_\lambda}{\sigma}$	Line ID				
λ_{obs}	W_λ	σ_{ph}	σ_{cont}		λ_{obs}	W_λ	σ_{ph}	σ_{cont}			Ion	λ_{rest}	$\Delta\lambda$	z_{abs}	Δv
(Å)	(Å)	(Å)	(Å)	Flag	(Å)	(Å)	(Å)	(Å)	(Å)	(11)	(12)	(Å)	(Å)	(15)	(km s ⁻¹)
(1)	(2)	(3)	(4)	(5)	(6)	(7)	(8)	(9)	(10)	(11)	(12)	(13)	(14)	(15)	(16)
2543.31	0.52	0.19	0.52		2542.42	0.62	0.06	0.62	0.10	0.11
2564.01	0.42	0.17	0.42	Σ	2563.59	1.43	0.09	0.65	1.01	1.27
...	1	2214.21	0.38	0.05	0.38
...	2	2431.14	1.05	0.08	0.52
2584.73	2.54	0.20	0.13		2583.74	2.90	0.06	0.07	0.36	1.41	H I ^c	1215.67	0.00	1.12536	...
2739.03	1.38	0.24	0.02		2737.96	1.29	0.06	0.16	-0.09	-0.32
2766.69	1.80	0.22	0.25		2765.94	1.97	0.06	0.01	0.17	0.50
2796.37	2.13	0.28	0.49	Σ	2792.87	2.13	0.08	0.07	0.00	0.00
...	1	2789.36	0.73	0.05	0.00
...	2	2793.04	0.07	0.03	0.07
...	3	2796.31	1.33	0.05	0.00	Mg II	2796.35	-0.04	0	...
2804.72	2.07	0.25	0.18	Σ	2805.04	2.00	0.07	0.13	-0.07	-0.20
...	1	2803.47	1.38	0.05	0.03	Mg II	2803.53	-0.06	0	...
...	2	2806.66	0.62	0.05	0.13
2853.44	1.75	0.19	0.10		2853.67	2.07	0.04	0.00	0.32	1.51	Mg I	2852.96	0.71	0	...
2868.64	1.57	0.23	0.15		2868.80	1.73	0.06	0.03	0.16	0.56	N I	1199.55	-0.98	1.39238	-2214
2885.65	1.43	0.19	0.11		2885.22	1.89	0.05	0.03	0.46	2.04	Si III	1206.50	-1.19	1.39238	-2235
2908.28	20.77	0.28	1.23		2908.35	20.65	0.06	0.94	-0.13	-0.08	H I	1215.67	0.00	1.39238	-2112
2962.79	<0.65	0.13	0.10		2962.35	0.70	0.05	0.03	>0.05	>0.29	N V	1238.82	-0.94	1.39238	-2252
2972.31	<0.70	0.14	0.10		2972.31	0.11	0.04	0.03	>-0.59	>-3.29	N V	1242.81	-0.96	1.39238	-2209
3014.46	2.85	0.30	0.74		3014.17	2.62	0.05	0.04	-0.22	-0.28	Si II	1260.42	-1.24	1.39238	-2235
3114.81	4.07	0.58	0.03	Σ	3116.33	4.12	0.13	0.21	0.05	0.08
...	1	3113.87	2.58	0.12	0.21	O I	1302.17	-1.42	1.39238	-2248
...	2	3118.92	1.54	0.06	0.05	Si II	1304.37	-1.63	1.39238	-2269
MRC 1118+128 ($z_e = 0.685$)															
1733.75	<4.35	0.87	0.00		1734.14	0.66	0.15	0.02	>-3.69	>-4.18	O VI	1031.93	-0.17	0.68065	-805
1861.67	4.41	0.92	0.01		1862.05	1.82	0.37	0.01	-2.59	-2.61	Al III	1862.79	-1.12	0	...

Table 2—Continued

STIS				Blend	FOS				ΔW_λ	$\frac{\Delta W_\lambda}{\sigma}$	Line ID				
λ_{obs}	W_λ	σ_{ph}	σ_{cont}		λ_{obs}	W_λ	σ_{ph}	σ_{cont}			Ion	λ_{rest}	$\Delta\lambda$	z_{abs}	Δv
(Å)	(Å)	(Å)	(Å)	Flag	(Å)	(Å)	(Å)	(Å)	(Å)	(11)	(12)	(Å)	(Å)	(15)	(km s ⁻¹)
(1)	(2)	(3)	(4)	(5)	(6)	(7)	(8)	(9)	(10)	(11)	(12)	(13)	(14)	(15)	(16)
2025.81	<1.70	0.34	0.00		2025.93	1.21	0.15	0.03	> -0.49	> -1.31	Si III	1206.50	-1.77	0.68065	-1037
2045.55	0.88	0.18	0.00		2043.12	1.38	0.08	0.06	0.50	2.43	H I	1215.67	0.00	0.68065	-774
2081.93	<0.85	0.17	0.00		2081.93	0.65	0.13	0.04	> -0.20	> -0.92	N V	1238.82	0.09	0.68065	-788
2384.61	1.11	0.45	1.11		2383.08	0.42	0.19	0.42	-0.69	-0.54	Fe II	2382.76	0.32	0	...
2586.12	<1.40	0.28	0.18		2586.35	1.12	0.15	0.16	> -0.28	> -0.70	Fe II	2586.65	-0.30	0	...
2602.61	2.03	0.28	0.28	Σ	2603.21	1.75	0.15	0.26	-0.28	-0.57
...	1	2600.77	1.04	0.12	0.24	C IV	1548.19	-1.20	0.68065	-912
...	2	2607.11	0.72	0.09	0.10	C IV	1550.77	0.81	0.68065	-682
2805.00	2.15	0.47	0.07	Σ	2799.98	2.72	0.29	0.21	0.57	0.95
...	1	2796.53	1.14	0.16	0.01	Mg II	2796.35	0.18	0	...
...	2	2803.82	1.58	0.24	0.20	Mg II	2803.53	0.29	0	...
PG 1241+176 ($z_e = 1.273$)															
1872.15	2.12	0.38	0.01						Si III	1206.50	0.85	0.55102	...
1886.91	3.30	0.39	0.00						H I	1215.67	1.38	0.55102	...
2045.97	3.30	0.33	0.00						H I	923.15	1.13	1.21507	-7570
2071.91	4.31	0.39	0.01					
2113.33	1.83	0.24	0.00					
2139.40	1.05	0.21	0.00					
2172.67	3.70	0.32	0.01					
2193.67	1.67	0.24	0.31						N III	989.80	1.20	1.21507	-7570
2272.85	<0.95	0.19	0.11		2272.39	0.58	0.09	0.04	> -0.37	> -1.54	H I	1025.72	0.35	1.21507	-7690
2289.17	0.72	0.25	0.51		2286.64	0.37	0.10	0.37	-0.35	-0.51	O VI	1031.93	0.85	1.21507	-7625
2304.31	1.66	0.23	0.06	Σ	2302.77	1.38	0.15	0.33	-0.29	-0.65
...	1	2298.79	0.29	0.09	0.29	O VI	1037.62	0.40	1.21507	-7684
...	2	2304.15	1.09	0.12	0.17
2346.47	3.03	0.19	0.05	Σ	2344.42	3.32	0.10	0.20	-0.29	-1.27
...	1	Fe II ^d	2344.21	0.21	0	...

Table 2—Continued

STIS				Blend	FOS				ΔW_λ	$\frac{\Delta W_\lambda}{\sigma}$	Line ID				
λ_{obs}	W_λ	σ_{ph}	σ_{cont}		λ_{obs}	W_λ	σ_{ph}	σ_{cont}			Ion	λ_{rest}	$\Delta\lambda$	z_{abs}	Δv
(Å)	(Å)	(Å)	(Å)	Flag	(Å)	(Å)	(Å)	(Å)	(Å)	(11)	(12)	(Å)	(Å)	(15)	(km s ⁻¹)
(1)	(2)	(3)	(4)	(5)	(6)	(7)	(8)	(9)	(10)	(11)	(12)	(13)	(14)	(15)	(16)
...	2	O VI ^d	1031.93	-1.67	1.2735	-148
2359.57	1.68	0.15	0.21		2357.80	1.81	0.09	0.19	0.12	0.36	O VI	1037.62	-1.23	1.2735	-90
2368.12	0.86	0.14	0.16		2367.00	0.69	0.06	0.02	-0.17	-0.78	Si II	1526.71	-0.95	0.55102	...
2373.47	<0.75	0.15	0.04		2374.17	0.33	0.06	0.02	> -0.42	> -2.51	Fe II	2374.46	-0.29	0	...
2384.08	0.82	0.17	0.01		2382.81	0.97	0.10	0.16	0.15	0.58	Fe II	2382.76	0.05	0	...
2403.27	1.46	0.19	0.01	Σ	2402.16	2.84	0.16	0.48	1.38	2.55
...	1	2401.28	1.70	0.09	0.34	C IV	1548.19	0.00	0.55102	...
...	2	2404.04	1.13	0.13	0.34	C IV	1550.77	-1.23	0.55102	...
2424.05	1.59	0.18	0.03		2422.63	1.55	0.07	0.04	-0.04	-0.23
2457.34	1.42	0.18	0.07		2455.95	1.24	0.08	0.00	-0.19	-0.88
2503.81	1.08	0.16	0.06		2502.34	1.50	0.08	0.01	0.42	2.32
2509.76	<0.85	0.17	0.03		2510.07	0.33	0.07	0.00	> -0.52	> -2.79
2588.02	1.35	0.22	0.00		2585.75	0.98	0.08	0.45	-0.37	-0.74	Fe II	2586.65	-0.90	0	...
2601.27	0.67	0.16	0.00		2600.12	0.72	0.07	0.04	0.05	0.28	Fe II	2600.17	-0.05	0	...
2643.01	<0.85	0.17	0.00		2643.22	0.33	0.07	0.02	> -0.52	> -2.81	Si II	1193.29	0.00	1.21507	-7736
2650.76	<0.90	0.18	0.00		2650.37	0.59	0.06	0.03	> -0.31	> -1.61
2658.51	<0.85	0.17	0.00		2658.96	0.52	0.07	0.02	> -0.33	> -1.78	N I	1200.22	0.39	1.21507	-7692
2695.21	1.21	0.14	0.00		2692.79	1.16	0.08	0.05	-0.05	-0.27	H I	1215.67	-0.00	1.21507	-7736
2706.59	0.68	0.15	0.00		2705.54	0.50	0.06	0.05	-0.18	-1.05
2740.67	<0.75	0.15	0.08		2740.15	0.56	0.06	0.09	> -0.19	> -0.94
2763.88	1.97	0.16	0.49		2761.62	1.97	0.06	0.39	-0.00	-2.78	H I	1215.67	0.00	1.2735	-173
2798.19	0.78	0.12	0.01		2796.58	0.98	0.05	0.00	0.20	1.49	Mg II	2796.35	0.23	0	...
2804.66	0.94	0.13	0.00		2803.67	0.88	0.05	0.01	-0.06	-0.43	Mg II	2803.53	0.14	0	...
2852.32	<0.75	0.15	0.00		2852.45	0.45	0.06	0.00	> -0.30	> -1.86	Mg I	2852.96	-0.51	0	...
PG 1309+355 ($z_e = 0.184$)															
1827.00	6.19	0.25	2.35		1826.09	4.01	0.10	0.87	-2.17	-0.86	C IV	1549.49 ^a	0.00	0.17852	-1393
2344.95	<0.85	0.17	0.03		2344.28	0.35	0.08	0.00	> -0.50	> -2.63	Fe II	2344.21	0.07	0	...

Table 2—Continued

STIS				Blend	FOS				ΔW_λ	$\frac{\Delta W_\lambda}{\sigma}$	Line ID				
λ_{obs}	W_λ	σ_{ph}	σ_{cont}		λ_{obs}	W_λ	σ_{ph}	σ_{cont}			Ion	λ_{rest}	$\Delta\lambda$	z_{abs}	Δv
(Å)	(Å)	(Å)	(Å)	Flag	(Å)	(Å)	(Å)	(Å)	(Å)	(11)	(12)	(Å)	(Å)	(15)	(km s ⁻¹)
(1)	(2)	(3)	(4)	(5)	(6)	(7)	(8)	(9)	(10)	(11)	(12)	(13)	(14)	(15)	(16)
2383.23	1.19	0.19	0.04		2382.98	0.56	0.09	0.00	-0.63	-2.94	Fe II	2382.76	0.22	0	...
2586.57	<0.85	0.17	0.05		2586.76	0.46	0.08	0.00	> -0.39	> -2.01	Fe II	2586.65	0.11	0	...
2600.50	0.83	0.16	0.09		2600.47	0.74	0.10	0.00	-0.09	-0.40	Fe II	2600.17	0.30	0	...
2797.62	0.85	0.14	0.00		2795.62	0.91	0.09	0.00	0.06	0.36	Mg II	2796.35	-0.73	0	...
2803.44	0.81	0.16	0.06		2803.45	0.77	0.09	0.00	-0.05	-0.23	Mg II	2803.53	-0.08	0	...
PG 1351+640 ($z_e = 0.0882$)															
1682.33	8.97	0.25	0.07		1682.54	7.97	0.11	1.44	-1.00	-0.68	C IV	1549.49 ^a	0.00	0.08573	-643
2345.77	1.05	0.11	0.00		2344.37	1.25	0.09	0.03	0.20	1.30	Fe II	2344.21	0.16	0	...
2376.14	0.82	0.11	0.00		2374.34	0.75	0.08	0.06	-0.08	-0.53	Fe II	2374.46	-0.12	0	...
2384.38	1.23	0.11	0.00		2382.66	1.36	0.09	0.06	0.13	0.86	Fe II	2382.76	-0.10	0	...
2578.86	0.23	0.10	0.23		2576.92	0.22	0.07	0.22	-0.01	-0.01	Mn II	2576.88	-0.04	0	...
2588.53	0.99	0.09	0.06		2584.74	1.30	0.08	0.10	0.31	1.82	Fe II	2586.65	-1.91	0	...
2601.59	1.48	0.11	0.12		2600.36	1.44	0.06	0.08	-0.04	-0.18	Fe II	2600.17	0.19	0	...
2798.29	2.07	0.10	0.02		2796.33	1.89	0.06	0.11	-0.17	-1.06	Mg II	2796.35	-0.02	0	...
2804.48	2.09	0.11	0.01		2803.44	1.75	0.06	0.11	-0.34	-2.04	Mg II	2803.53	-0.09	0	...
2853.89	0.70	0.12	0.02		2853.17	0.69	0.06	0.07	-0.02	-0.10	Mg I	2852.96	0.21	0	...
3007.80	<0.70	0.14	0.00		3007.07	0.25	0.05	0.00	> -0.45	> -3.03
PG 1411+442 ($z_e = 0.0896$)															
1680.19	15.11	0.23	0.84		1680.17	15.28	0.15	0.05	0.17	0.19	C IV	1549.49 ^a	1.39	0.08435	-1451
1702.63	<0.75	0.15	0.00		1702.48	0.25	0.06	0.00	> -0.50	> -3.09
2345.63	0.50	0.09	0.06		2344.35	0.80	0.09	0.03	0.31	2.15	Fe II	2344.21	0.14	0	...
2383.56	0.66	0.10	0.09		2382.67	0.80	0.09	0.05	0.14	0.83	Fe II	2382.76	-0.09	0	...
2587.04	0.64	0.09	0.12		2586.56	0.56	0.09	0.05	-0.09	-0.50	Fe II	2586.65	-0.09	0	...
2600.48	0.84	0.09	0.13		2599.94	0.90	0.09	0.14	0.06	0.26	Fe II	2600.17	-0.23	0	...
2796.92	0.94	0.09	0.02		2796.17	1.18	0.08	0.00	0.24	1.97	Mg II	2796.35	-0.18	0	...
2803.93	1.07	0.09	0.07		2803.40	0.80	0.06	0.00	-0.27	-2.10	Mg II	2803.53	-0.13	0	...
PG 1425+260 ($z_e = 0.366$)															

Table 2—Continued

STIS				Blend	FOS				ΔW_λ	$\frac{\Delta W_\lambda}{\sigma}$	Line ID				
λ_{obs}	W_λ	σ_{ph}	σ_{cont}		λ_{obs}	W_λ	σ_{ph}	σ_{cont}			Ion	λ_{rest}	$\Delta\lambda$	z_{abs}	Δv
(Å)	(Å)	(Å)	(Å)	Flag	(Å)	(Å)	(Å)	(Å)	(Å)	(Å)	(12)	(Å)	(Å)	(15)	(km s ⁻¹)
(1)	(2)	(3)	(4)	(5)	(6)	(7)	(8)	(9)	(10)	(11)	(12)	(13)	(14)	(15)	(16)
1652.50	3.12	0.51	0.06		1651.85	3.35	0.21	0.35	0.23	0.35	H I	1215.67	0.00	0.3588	-1584
1664.96	1.37	0.48	1.37	Σ	1666.11	0.66	0.09	0.49	-0.71	-0.46
...	1	1661.43	0.44	0.07	0.44	H I	1215.67	0.00	0.36322	+149
...	2	1670.79	0.22	0.06	0.22	Al II	1670.79	0.00	0	...
1684.58	<2.00	0.40	0.30		1684.58	1.49	0.21	0.39	> -0.51	> -0.76	N v	1238.82	1.27	0.3588	-1358
1689.48	<2.45	0.49	0.21		1689.48	1.24	0.17	0.35	> -1.21	> -1.83	N v	1242.80	0.76	0.3588	-1448
2102.73	0.60	0.15	0.54	Σ	2103.74	1.25	0.37	0.31	-0.65	-0.88
...	1	2101.78	0.25	0.22	0.15	C IV	1548.20	0.00	0.3588	-1857
...	2	2105.69	1.00	0.30	0.27	C IV	1550.77	-0.43	0.3588	-1797
2116.39	0.44	0.15	0.35	Σ	2112.97	1.29	0.08	0.34	-0.85	-1.64
...	1	2110.55	0.78	0.07	0.26	C IV	1548.20	0.00	0.3638	-609
...	2	2115.38	0.51	0.04	0.22	C IV	1550.77	-1.34	0.3638	-421
2344.21	<1.30	0.26	0.00		2344.78	0.70	0.13	0.00	> -0.60	> -2.06	Fe II	2344.21	0.57	0	...
2384.69	1.15	0.25	0.00		2382.82	0.78	0.12	0.01	-0.36	-1.32	Fe II	2382.76	0.06	0	...
2587.85	1.51	0.25	0.00		2586.65	1.09	0.10	0.01	-0.42	-1.58	Fe II	2586.65	0.00	0	...
2599.78	<0.95	0.19	0.00		2600.05	0.77	0.09	0.00	> -0.18	> -0.86	Fe II	2600.17	-0.12	0	...
2797.25	1.90	0.34	0.00	Σ	2799.73	1.96	0.18	0.14	0.06	0.15
...	1	2796.17	0.97	0.15	0.14	Mg II	2796.35	-0.18	0	...
...	2	2803.46	1.00	0.11	0.01	Mg II	2803.53	-0.07	0	...
3C 351 ($z_e = 0.37194$)															
1643.49	1.57	0.59	1.57		1645.20	0.61	0.12	0.00	Si III	1206.50	-1.12	0.36454	-1824
1660.10	3.78	0.40	0.68		1658.83	3.85	0.12	0.23	0.06	0.07	H I	1215.67	0.00	0.36454	-1621
1672.67	2.83	0.31	0.42	Σ	1669.01	1.86	0.15	0.83	-0.97	-0.97
...	1	1665.13	0.69	0.08	0.69	H I	1215.67	0.00	0.36972	-485
...	2	1671.23	1.17	0.13	0.47	Al II	1670.79	0.44	0	...
1690.64	<1.70	0.34	0.26		1690.19	1.04	0.10	0.14	> -0.66	> -1.43	N v	1238.82	-0.23	0.36454	-1662
1694.42	0.88	0.39	0.88		1694.76	0.58	0.10	0.58	-0.30	-0.26	N v	1242.80	-1.10	0.36454	-1814

Table 2—Continued

STIS				Blend	FOS				ΔW_λ	$\frac{\Delta W_\lambda}{\sigma}$	Line ID				
λ_{obs}	W_λ	σ_{ph}	σ_{cont}		λ_{obs}	W_λ	σ_{ph}	σ_{cont}			Ion	λ_{rest}	$\Delta\lambda$	z_{abs}	Δv
(Å)	(Å)	(Å)	(Å)	Flag	(Å)	(Å)	(Å)	(Å)	(Å)	(11)	(12)	(Å)	(Å)	(15)	(km s ⁻¹)
(1)	(2)	(3)	(4)	(5)	(6)	(7)	(8)	(9)	(10)	(11)	(12)	(13)	(14)	(15)	(16)
1863.62	<2.00	0.40	0.12		1864.38	0.65	0.09	0.09	> -1.35	> -3.09	Al III	1862.79	-0.12	0	...
1889.89	<1.85	0.37	0.10		1890.52	0.33	0.06	0.08	> -1.52	> -3.84	C IV	1548.19	0.00	0.22112	...
2039.81	<1.40	0.28	0.09		2040.00	0.49	0.07	0.10	> -0.91	> -2.86	C IV	1548.19	0.00	0.31767	...
2115.05	3.71	0.22	0.39		2113.09	3.79	0.09	0.27	0.08	0.15	C IV	1549.49 ^a	0.52	0.36454	-1798
2345.25	0.93	0.20	0.00		2344.38	0.99	0.11	0.05	0.05	0.23	Fe II	2344.21	0.17	0	...
2383.74	1.06	0.18	0.00		2382.84	1.18	0.11	0.09	0.12	0.52	Fe II	2382.76	0.08	0	...
2586.30	0.75	0.23	0.75		2586.73	0.39	0.09	0.39	-0.36	-0.41	Fe II	2586.65	0.08	0	...
2601.00	2.17	0.23	0.88		2600.05	1.10	0.09	0.01	-1.07	-1.17	Fe II	2600.17	-0.12	0	...
2797.22	2.12	0.22	0.21		2796.02	1.66	0.10	0.00	-0.45	-1.39	Mg II	2796.35	-0.33	0	...
2803.33	1.43	0.22	0.11		2803.27	1.37	0.10	0.00	-0.06	-0.25	Mg II	2803.53	-0.26	0	...
2854.26	<1.25	0.25	0.02		2853.70	0.55	0.09	0.00	> -0.70	> -2.63	Mg I	2852.96	0.71	0	...
2910.46	1.06	0.22	0.03		2910.11	<0.50	0.10	0.00	<0.56	<2.30	Fe II	2382.76	-0.13	0.22152	...
PG 1718+481 ($z_e = 1.084$)															
2005.01	<0.95	0.19	0.00		2004.62	0.66	0.06	0.00	> -0.29	> -1.46
2069.32	1.35	0.17	0.00		2068.04	1.18	0.04	0.00	-0.17	-0.97	H I	1215.67	-0.24	0.70135	...
2085.18	1.13	0.16	0.00		2084.32	0.85	0.04	0.00	-0.28	-1.70	H I	1025.72	-0.49	1.03253	-7563
2097.80	<0.50	0.10	0.00		2097.30	0.31	0.02	0.00	> -0.19	> -1.86	O VI	1031.93	-0.13	1.03253	-7512
2109.57	0.65	0.13	0.00		2108.30	0.78	0.04	0.00	0.13	0.96	O VI	1037.02 ^e	-0.69	1.03253	-7419
2120.19	0.81	0.16	0.00		2120.97	0.52	0.03	0.00	-0.29	-1.78
2141.33	0.55	0.13	0.00		2140.59	0.37	0.03	0.00	-0.18	-1.35	H I	1025.72	-0.35	1.08725	+419
2153.57	<0.30	0.06	0.00		2153.57	0.14	0.04	0.00	> -0.16	> -2.22	O VI	1031.93	-0.33	1.08725	+422
2165.75	<0.30	0.06	0.00		2165.75	0.17	0.04	0.00	> -0.13	> -1.80	O VI	1037.62	-0.02	1.08725	+464
2176.69	<0.65	0.13	0.00		2176.60	0.39	0.04	0.00	> -0.26	> -1.91
2204.54	<0.60	0.12	0.00		2205.09	0.38	0.03	0.00	> -0.22	> -1.78
2212.28	<0.60	0.12	0.00		2212.54	0.52	0.04	0.00	> -0.08	> -0.63
2269.54	<0.65	0.13	0.00		2269.28	0.61	0.05	0.00	> -0.04	> -0.29	C II	1334.53	-1.22	0.70135	...
2277.28	<0.60	0.12	0.00		2277.37	0.51	0.07	0.00	> -0.09	> -0.65

Table 2—Continued

STIS				Blend Flag	FOS				ΔW_λ (Å)	$\frac{\Delta W_\lambda}{\sigma}$ (11)	Line ID				
λ_{obs} (Å) (1)	W_λ (Å) (2)	σ_{ph} (Å) (3)	σ_{cont} (Å) (4)		λ_{obs} (Å) (6)	W_λ (Å) (7)	σ_{ph} (Å) (8)	σ_{cont} (Å) (9)			Ion (12)	λ_{rest} (Å) (13)	$\Delta\lambda$ (Å) (14)	z_{abs} (15)	Δv (km s ⁻¹) (16)
2302.46	1.52	0.18	0.00		2301.65	0.95	0.07	0.00	-0.57	-2.95
2345.38	<0.60	0.12	0.00		2344.66	0.72	0.06	0.00	>0.12	>0.89	Fe II	2344.21 ^e	0.45	0	...
2357.77	<0.55	0.11	0.00		2358.30	0.42	0.07	0.00	>-0.13	>-1.00
2375.90	0.69	0.12	0.01	Σ	2375.98	0.85	0.08	0.01	0.16	1.06
...	1	2374.78	0.52	0.06	0.01	Fe II	2374.46	0.32	0	...
...	2	2377.25	0.33	0.05	0.00
2384.08	0.99	0.13	0.10		2382.83	0.75	0.05	0.00	-0.24	-1.39	Fe II	2382.76	0.07	0	...
2399.80	0.71	0.11	0.09		2399.03	1.06	0.06	0.06	0.36	2.05
2429.00	<0.55	0.11	0.04		2429.33	0.44	0.05	0.02	>-0.11	>-0.85
2441.13	0.43	0.10	0.01		2439.93	0.56	0.06	0.00	0.14	1.16
2471.20	1.28	0.13	0.00		2470.89	1.06	0.06	0.02	-0.23	-1.60	H I	1215.67	0.00	1.03253	-7493
2498.54	1.70	0.11	0.07	Σ	2496.04	2.17	0.09	0.08	0.47	2.67
...	1	2493.75	0.67	0.05	0.01	C IV	1548.20	0.00	0.6108	...
...	2	2498.38	1.50	0.07	0.08	C IV	1550.77	0.48	0.6108	...
2514.83	0.46	0.07	0.00		2513.26	0.99	0.05	0.27	0.53	1.88	Si I	1562.00	-2.73	0.6108	...
2537.43	<0.35	0.07	0.07		2537.42	0.72	0.04	0.03	>0.37	<u>>3.34</u>	<u>H I</u>	1215.67	0.00	1.08726	<u>+469</u>
2587.64	0.34	0.07	0.00		2586.46	0.41	0.04	0.10	0.07	0.87	Fe II	2586.65	-0.19	0	...
2600.73	0.71	0.09	0.03		2599.81	0.88	0.05	0.10	0.17	1.61	Fe II	2600.17	-0.36	0	...
2796.73	1.78	0.12	0.00		2796.05	1.72	0.06	0.00	-0.06	-0.45	Mg II	2796.35	-0.30	0	...
2802.44	1.17	0.11	0.00		2804.33	1.39	0.07	0.00	0.22	1.69	Mg II	2803.53	0.80	0	...
2853.68	<0.70	0.14	0.00		2853.13	0.36	0.05	0.00	>-0.34	>-2.29	Mg I	2852.96	0.17	0	...
3145.46	<1.30	0.26	0.00		3146.18	0.52	0.05	0.00	>-0.78	>-2.95	C IV	1548.19	-0.26	1.03253	-7547
3151.67	<1.15	0.23	0.00		3151.73	0.49	0.05	0.00	>-0.66	>-2.80	C IV	1550.77	-0.56	1.03253	-7518
PKS 2135-14 ($z_e = 0.20036$)															
1862.13	3.18	0.19	0.26		1861.54	4.70	0.10	0.30	1.52	<u>3.37</u>	<u>C IV^f</u>	1549.49 ^a	0.00	0.20140	<u>+257</u>
2012.95	<1.55	0.31	0.00		2012.87	0.54	0.10	0.00	>-1.01	>-3.10
2804.06	1.10	0.20	0.00		out of range			Mg II	2803.53	0.53	0	...

Table 2—Continued

STIS				Blend	FOS				ΔW_λ	$\frac{\Delta W_\lambda}{\sigma}$	Line ID				
λ_{obs}	W_λ	σ_{ph}	σ_{cont}		λ_{obs}	W_λ	σ_{ph}	σ_{cont}			Ion	λ_{rest}	$\Delta\lambda$	z_{abs}	Δv
(Å)	(Å)	(Å)	(Å)	Flag	(Å)	(Å)	(Å)	(Å)	(Å)	(Å)	(12)	(Å)	(Å)	(15)	(km s ⁻¹)
(1)	(2)	(3)	(4)	(5)	(6)	(7)	(8)	(9)	(10)	(11)	(12)	(13)	(14)	(15)	(16)
MRC 2251-178 ($z_e = 0.06398$)															
1648.99	0.38	0.12	0.26	Σ	1647.14	1.65	0.06	0.20	1.27	<u>3.56</u>
...	1	1645.77	1.07	0.03	0.03	<u>C IV</u>	1548.19	0.00	0.06302	<u>-268</u>
...	2	1648.64	0.58	0.05	0.20	<u>C IV</u>	1550.77	0.13	0.06302	<u>-245</u>
1670.19	<0.90	0.18	0.07		1670.81	0.60	0.04	0.05	> -0.30	> -1.47	Al II	1670.79	0.02	0	...
1934.32	<0.90	0.18	0.04		1934.03	0.31	0.04	0.02	> -0.59	> -3.11
2345.29	1.27	0.17	0.29		2343.91	0.42	0.12	0.12	-0.85	-2.26	Fe II	2344.21	1.08	0	...
2376.42	0.81	0.11	0.03		2375.00	1.22	0.11	0.02	0.41	2.51	... ^g
2384.44	1.06	0.13	0.07		2382.79	1.22	0.11	0.02	0.16	0.85	Fe II	2382.76	1.68	0	...
2587.28	<0.50	0.10	0.03		2586.90	0.34	0.06	0.00	> -0.16	> -1.33	Fe II	2586.65	0.25	0	...
2602.77	0.67	0.11	0.03		2600.37	0.73	0.08	0.00	0.06	0.38	Fe II	2600.17	0.20	0	...
2798.44	0.75	0.11	0.05		2796.20	0.93	0.07	0.04	0.17	1.22	Mg II	2796.35	-0.15	0	...
2805.48	1.09	0.13	0.14		2803.33	0.98	0.07	0.02	-0.11	-0.54	Mg II	2803.53	-0.20	0	...
PG 2251+113 ($z_e = 0.3255$)															
1570.92	10.80	0.94	0.00		out of range			
2043.52	<0.85	0.17	0.00		2043.43	0.23	0.03	0.02	> -0.62	> -3.57
2054.65	0.92	0.16	0.06	Σ	2053.92	1.83	0.07	0.01	0.91	<u>4.96</u>
...	1	2052.12	0.95	0.03	0.00	<u>C IV</u>	1548.19	0.00	0.32549	<u>-1</u>
...	2	2055.48	0.88	0.06	0.01	<u>C IV</u>	1550.77	-0.05	0.32549	<u>-10</u>
2343.72	<1.15	0.23	0.00		2344.14	0.52	0.10	0.00	> -0.63	> -2.51	Fe II	2344.21	-0.08	0	...
2374.69	<1.15	0.23	0.00		2374.59	0.62	0.11	0.00	> -0.53	> -2.08	Fe II	2374.46	0.13	0	...
2382.43	<1.20	0.24	0.00		2382.85	0.71	0.10	0.00	> -0.49	> -1.88	Fe II	2382.77	0.08	0	...
2386.92	<1.10	0.22	0.00		2586.82	0.37	0.09	0.00	> -0.73	> -3.07	Fe II	2586.65	0.17	0	...
2599.32	<1.15	0.23	0.00		2600.03	0.80	0.09	0.00	> -0.35	> -1.42	Fe II	2600.17	-0.14	0	...
2798.26	2.33	0.35	0.00	Σ	2797.97	2.47	0.19	0.32	0.14	0.27
...	1	2793.75	0.41	0.08	0.00
...	2	2796.99	1.37	0.16	0.32	Mg II	2796.35	0.64	0	...

Table 2—Continued

STIS				Blend	FOS				ΔW_λ	$\frac{\Delta W_\lambda}{\sigma}$	Line ID				
λ_{obs}	W_λ	σ_{ph}	σ_{cont}		λ_{obs}	W_λ	σ_{ph}	σ_{cont}			Ion	λ_{rest}	$\Delta\lambda$	z_{abs}	Δv
(\AA)	(\AA)	(\AA)	(\AA)	Flag	(\AA)	(\AA)	(\AA)	(\AA)	(\AA)	(11)	(12)	(\AA)	(\AA)	(15)	(km s^{-1})
(1)	(2)	(3)	(4)	(5)	(6)	(7)	(8)	(9)	(10)	(11)	(12)	(13)	(14)	(15)	(16)
...	3	2803.59	0.69	0.08	0.00	Mg II	2803.53	0.06	0	...

Note. — See §2 of the text for a detailed explanation of the organization of this table and meaning of the columns.

^aMean wavelength of doublet; adopted when the doublet is unresolved in both the FOS and STIS spectra.

^bThe Si IV $\lambda 1393$ line at $z_a = 1.009$ in the spectrum of EX 0302–223 is contaminated by Galactic Mg II $\lambda 2803$.

^cThe Ly α line at $z_a = 1.125$ in the spectrum of QSO 0957+561A is contaminated by Galactic Fe II $\lambda 2586$.

^dIn the case of PG 1241+176, the Galactic Fe II $\lambda 2344$ line and the O VI $\lambda 1032$ line at $z_a = 1.2735$ are blended in both the STIS and FOS spectra.

^eIn the case of PG 1718+481, the O VI $\lambda 1037$ and Fe II $\lambda 2344$ lines appear to be blended with neighboring unidentified lines in both the STIS and FOS spectra.

^fThe C IV doublet at $z_a = 0.2014$ in the spectrum of PKS 2135–14 is slightly contaminated by the Galactic Al III $\lambda 1863$ line.

^gThe observed lines at $\lambda 2376$ and $\lambda 2384$ in the spectrum of MRC 2251–178 are unidentified. However, they are contaminated by the Galactic Fe II $\lambda 2344$ and $\lambda 2374$, respectively.

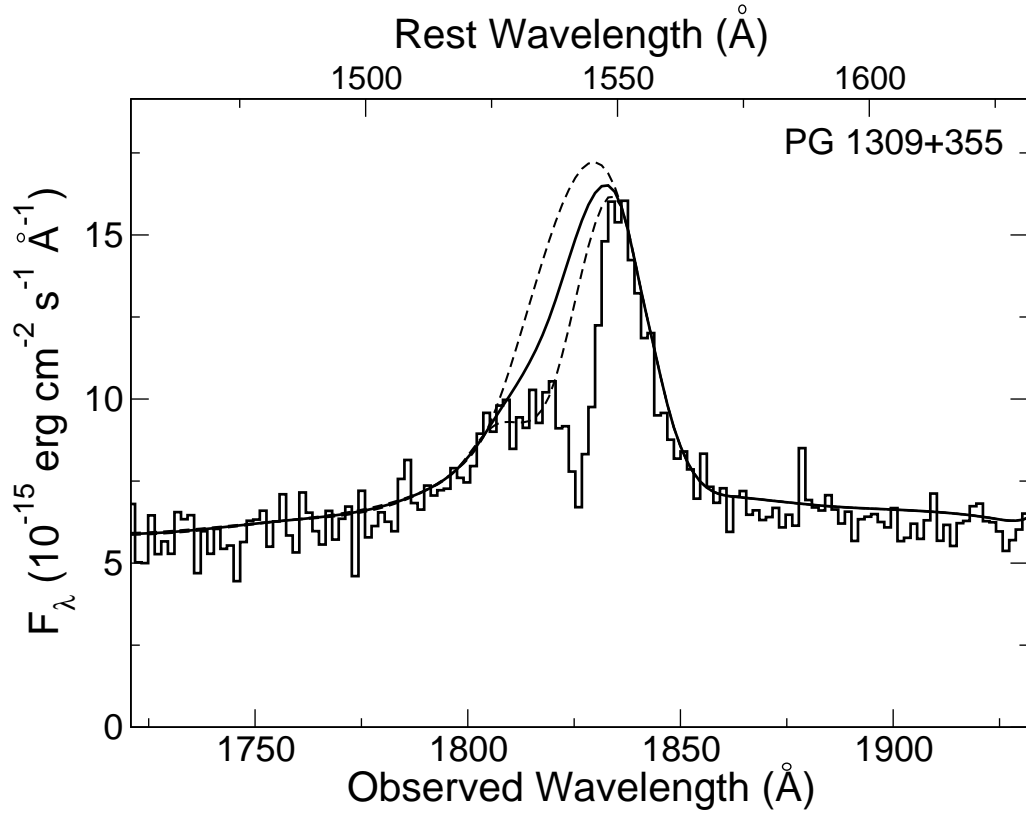


Fig. 1.— An example of extreme continuum fits to the STIS spectrum of a broad C IV emission line. We incorporate these uncertainties into our selection criteria of variable lines. An additional illustration using a FOS spectrum can be found in Figure 7.

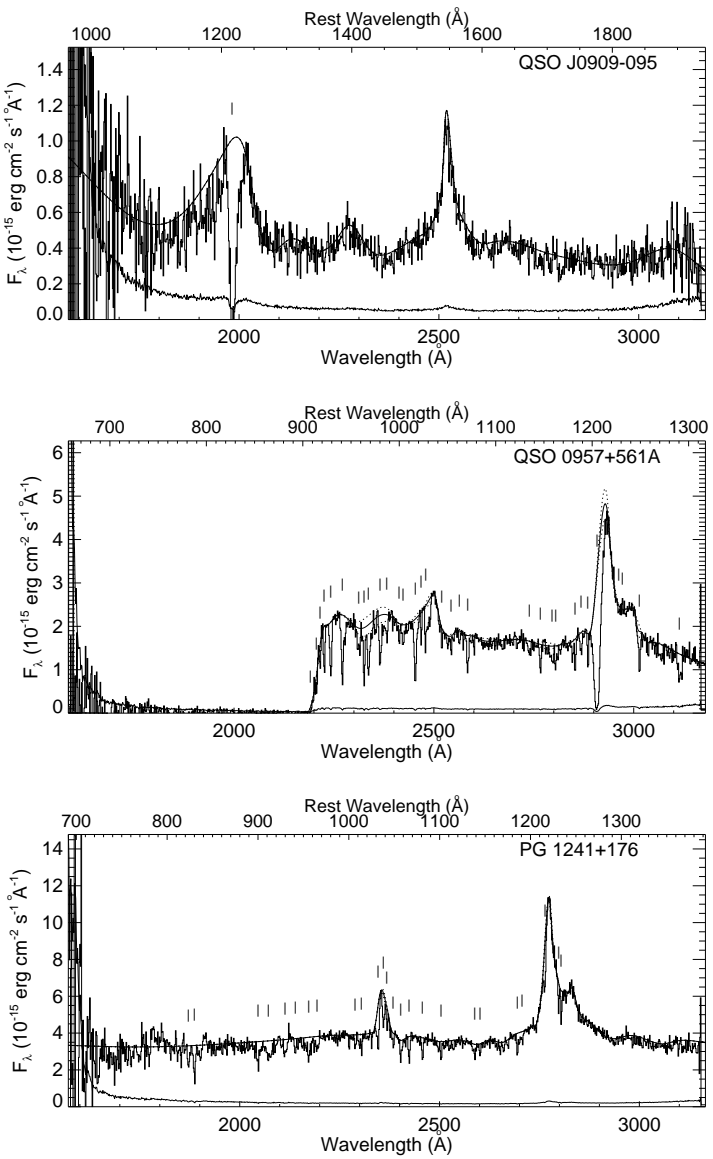
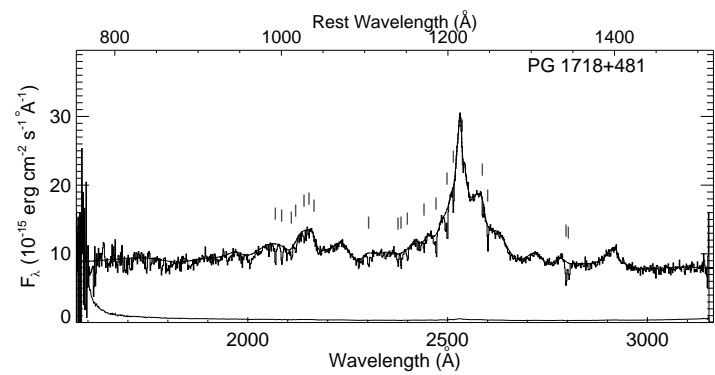
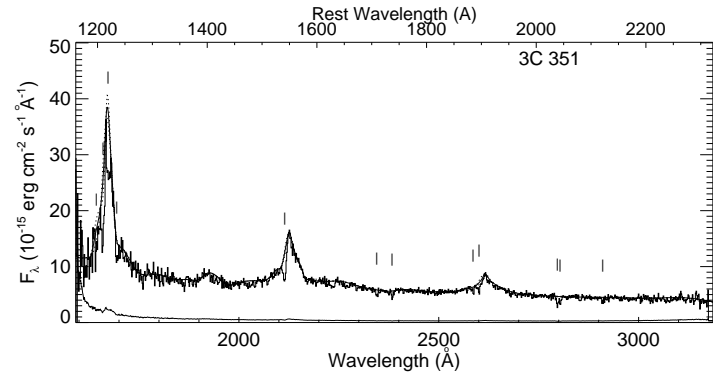
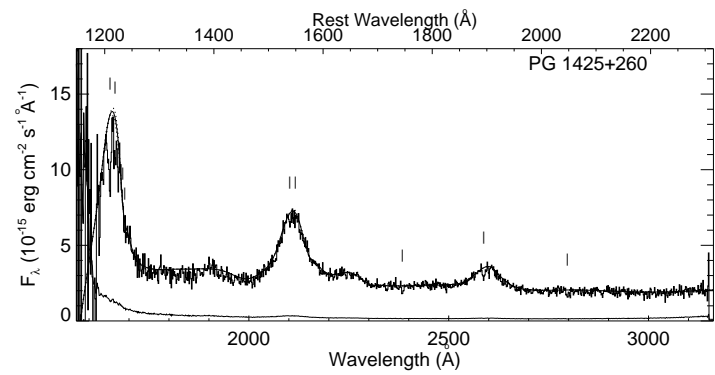
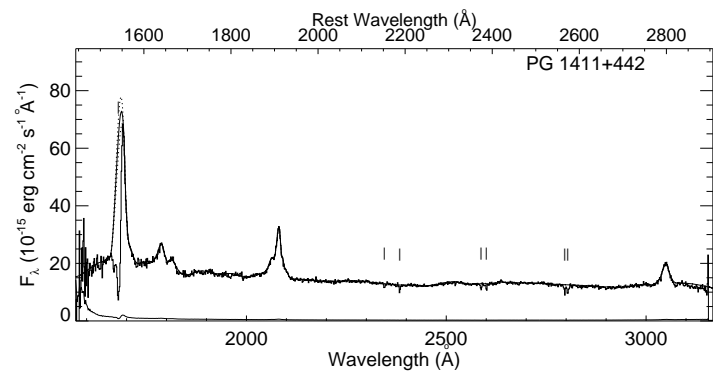
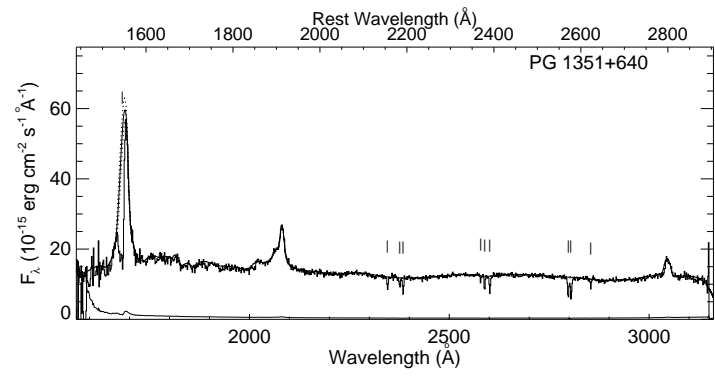
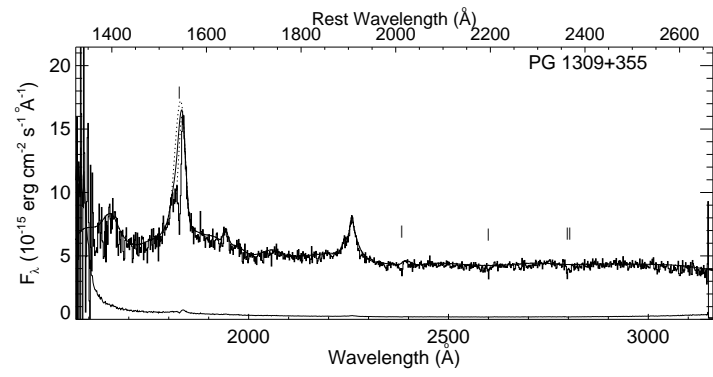


Fig. 2.— The STIS spectra of quasars observed in this survey with the best *effective* continuum fit superposed (the fit is not optimized in low- S/N regions near the ends of some of the spectra). The extreme continuum fits (see §2 of the text) are also shown as dotted lines. The lower trace in each panel shows the error bar spectrum. The tick marks show the detected absorption lines listed in Table 2

Fig. 2 (continued)



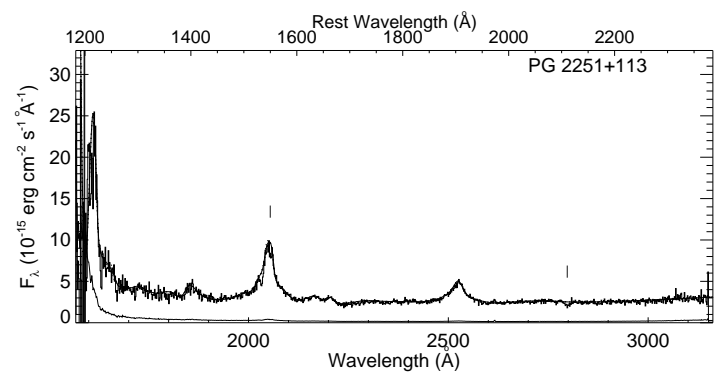
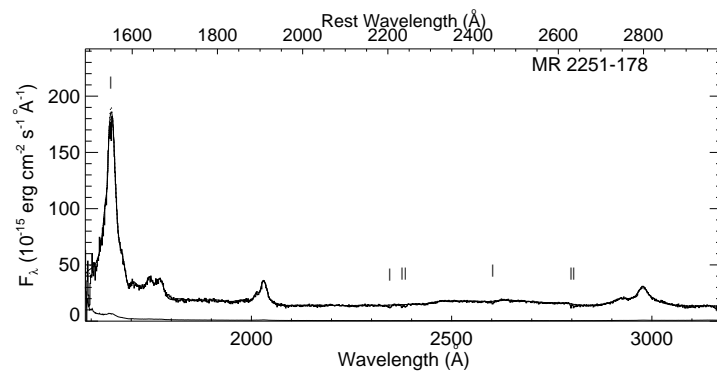
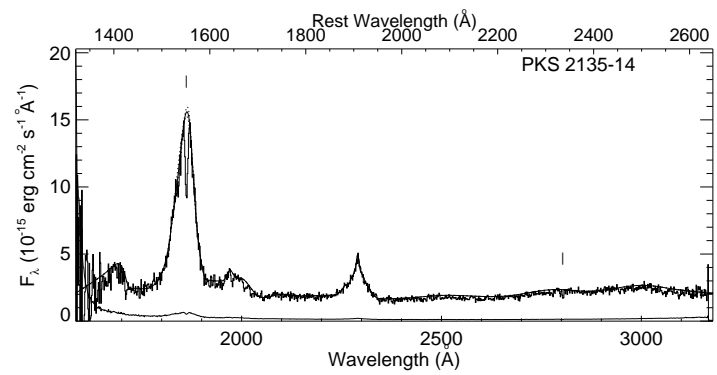


Fig. 2 (continued)

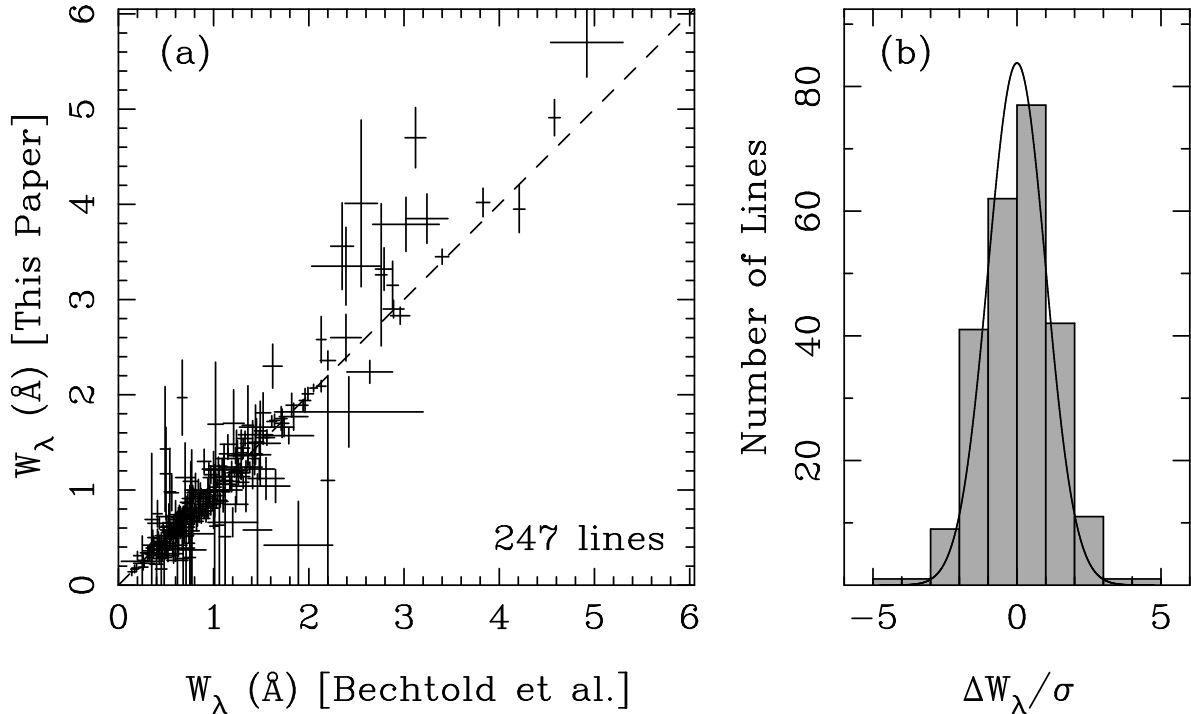


Fig. 3.— Comparison of the EWs of 247 lines that we have measured in FOS spectra with measurements of the same lines by Bechtold et al. (2002). (a) Our EW measurement plotted against that of Bechtold et al. (2002). The dashed line has unit slope and illustrates the good agreement between the two sets of measurements. In the interest of clarity, this plot shows only the range of observed EWs up to 6 Å; three lines with $6 \text{ \AA} < W_\lambda < 20 \text{ \AA}$ are omitted. (b) The distribution of the normalized deviation between the two measurements, namely $\Delta W_\lambda / \sigma \equiv [W_\lambda(\text{theirs}) - W_\lambda(\text{ours})] / (\sigma_{\text{theirs}}^2 + \sigma_{\text{ours}}^2)^{1/2}$. This histogram, which comprises all lines, appears symmetric about zero and includes five outliers with $|\Delta W_\lambda / \sigma| > 3$ (one is out of the range of the plot at $|\Delta W_\lambda / \sigma| \approx 8$). For comparison, we overplot as a solid line a Gaussian of unit standard deviation, which represents the *expected* distribution of $\Delta W_\lambda / \sigma$.

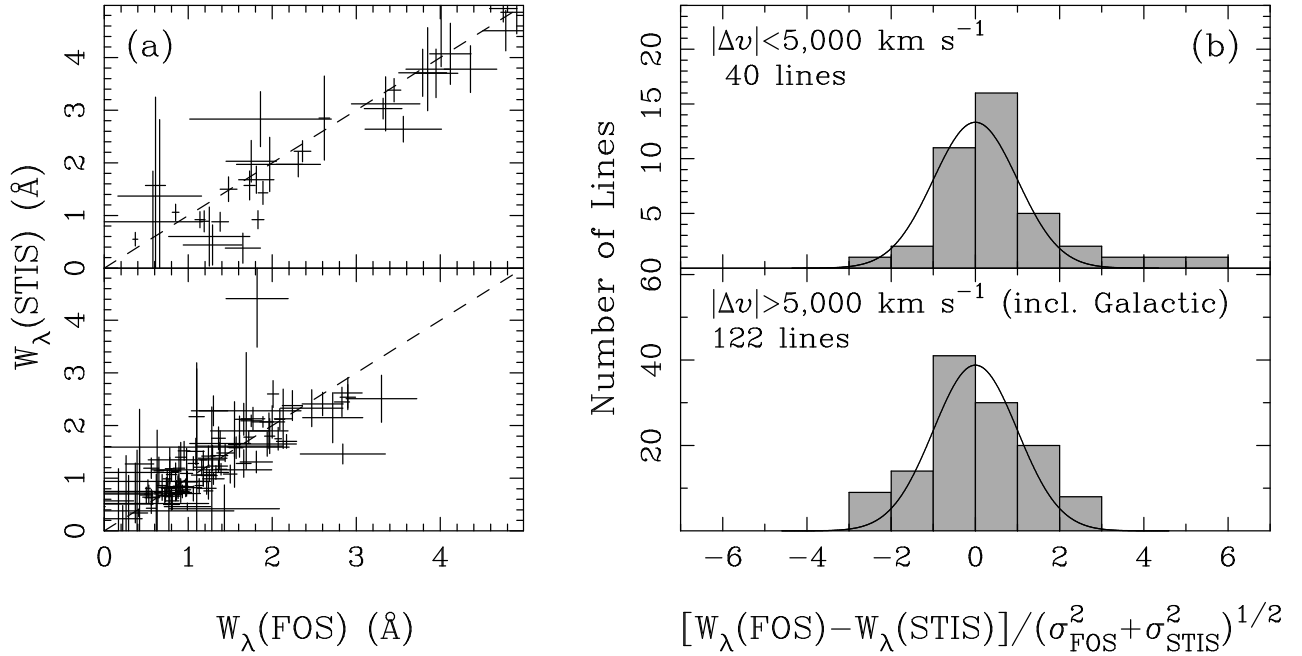


Fig. 4.— Distribution of differences between the EWs of the same lines as measured by the STIS and the FOS in two velocity bins relative to the quasar redshift: $|\Delta v| < 5,000 \text{ km s}^{-1}$ (associated lines; top panel) and $|\Delta v| > 5,000 \text{ km s}^{-1}$ (including Galactic and unidentified lines; bottom panel). See §2 of the text for an explanation of this division. Included in this figure are the two lines with STIS detections and FOS upper limits, bringing the total number of lines to 40 associated and 122 non-associated. (a) A plot of $W_\lambda(\text{STIS})$ vs $W_\lambda(\text{FOS})$ restricted to EW up to 5 \AA for clarity. The dashed line in each panel has unit slope. (b) The distribution of the EW differences normalized by the uncertainty, $[W_\lambda(\text{FOS}) - W_\lambda(\text{STIS})] / (\sigma_{\text{FOS}}^2 + \sigma_{\text{STIS}}^2)^{1/2}$. The error bars (σ_{STIS} and σ_{FOS}) include contributions from photon noise uncertainties and continuum placement uncertainties. The solid line overplotted on each histogram is a Gaussian of unit standard deviation, which is the distribution expected *a priori*, if the normalized EW differences are a result of measurement errors only.

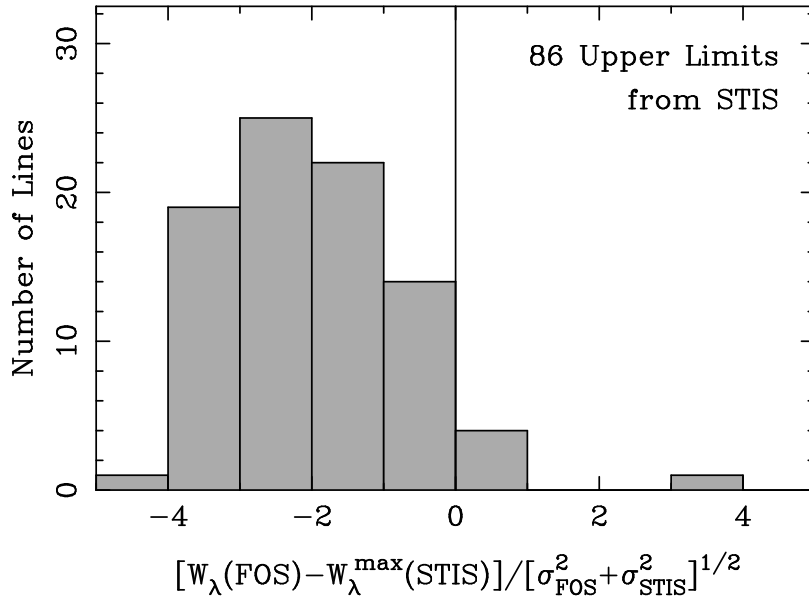


Fig. 5.— Distribution of the normalized EW differences of lines measured in FOS spectra but not detected in STIS spectra. This is analogous to the plot in the Figure 4b, but with $W_\lambda(\text{STIS})$ replaced by the 5σ upper limit $W_\lambda^{\text{max}}(\text{STIS})$. The 3.3σ outlier on the far right is a Ly α line in PG 1718+481 at $\Delta v = +469 \text{ km s}^{-1}$.

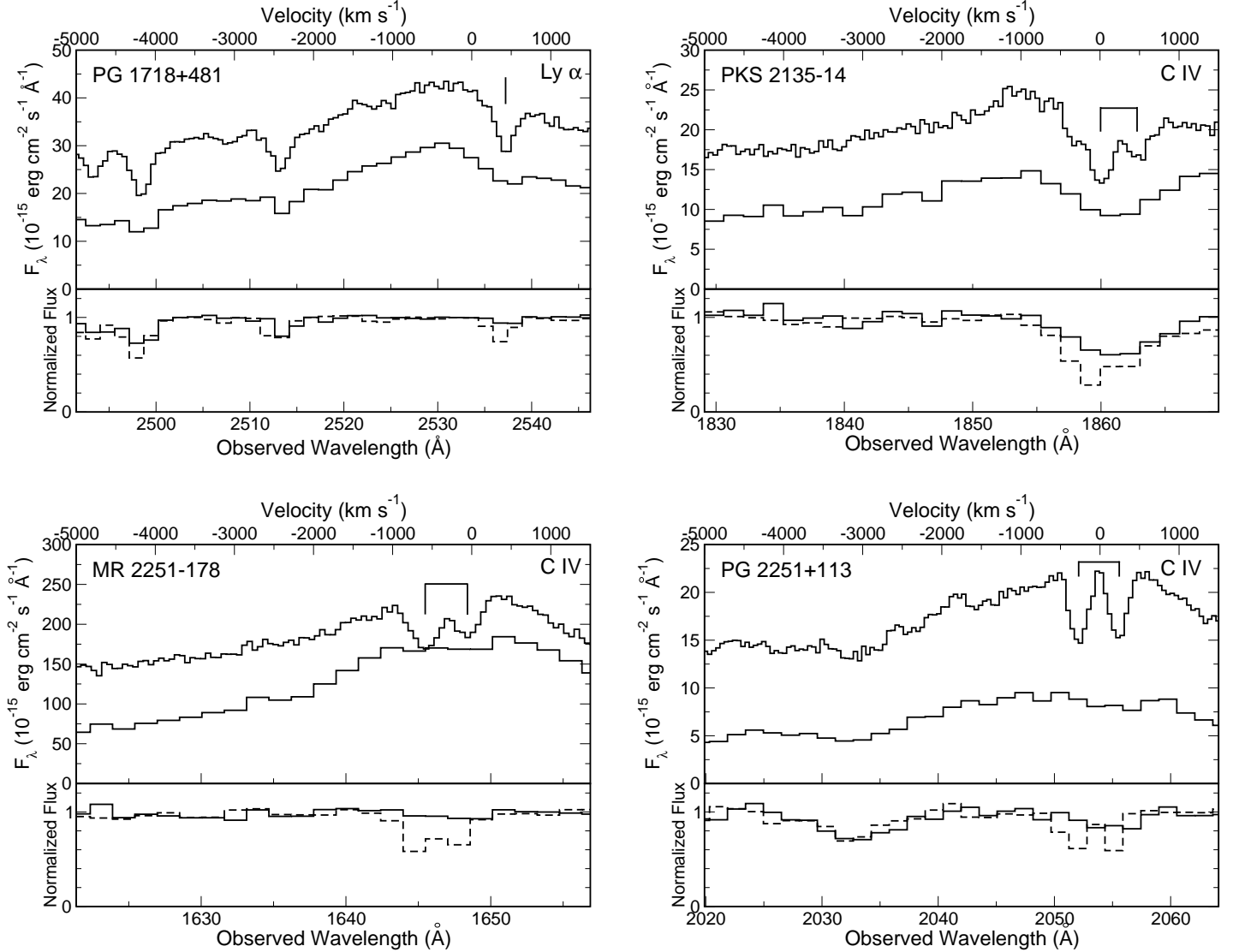


Fig. 6.— Visual illustration of the the variable NALs found in our variability survey. The top panel in each set shows STIS and FOS spectra overplotted. The FOS spectrum can be distinguished by its higher sampling rate and by the fact that it has been shifted upwards for clarity. The absorption lines of interest are identified by tick-marks. The bottom panel in each set shows the continuum-normalized spectra from the FOS (dashed line) and STIS (solid line). The FOS spectrum has been smoothed to the STIS resolution and resampled to the STIS wavelength scale to provide a fair comparison. The wavelength scales of the normalized spectra were aligned by comparing the observed wavelengths of Galactic, interstellar lines.

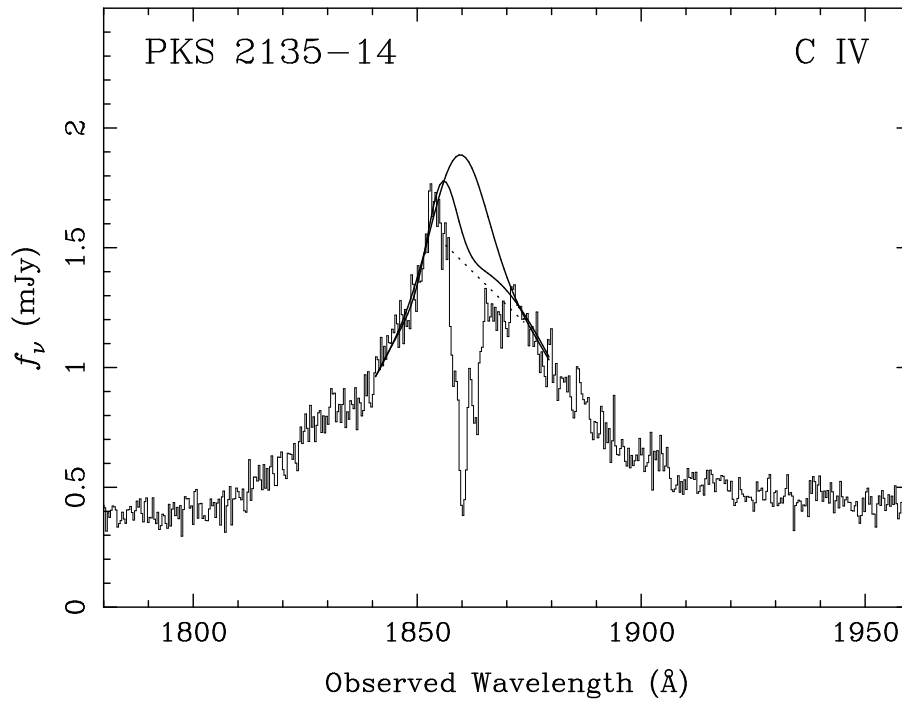


Fig. 7.— The C IV emission-line spectrum of PKS 2135–14 with two extreme *effective* continuum fits superposed as smooth, solid lines. The dotted line is a linear interpolation over the main absorption trough; it approximates the fit used by Bechtold et al. (2002) to measure the EW of the same absorption line.

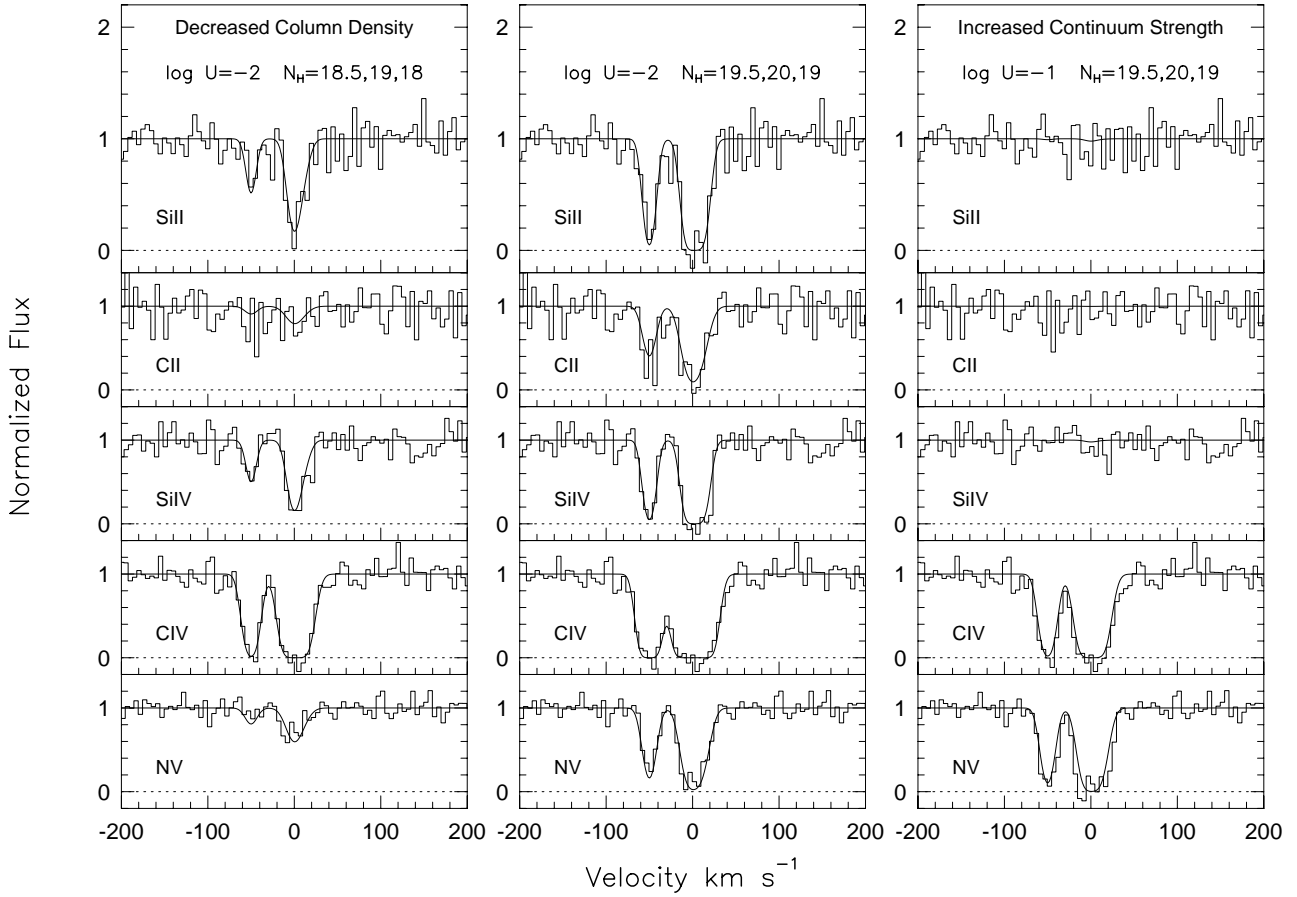


Fig. 8.— Results of simulations demonstrating the effect of bulk motion and changing continuum strength on a series of atomic transitions of a hypothetical NAL system. The details of the simulations are described in §4.3 of the text. The middle set of panels shows the initial state of the absorber. The set of panels on the left show the effect of decreasing the column density by an order of magnitude. The set of panels on the right show the effect of increasing the ionization parameter by an order of magnitude.